How Subduction Interface Roughness Influences the Occurrence of Large Interplate Earthquakes

Elenora van Rijsingen, Serge Lallemand, Michel Peyret, Diane Arcay, Arnauld Heuret, Francesca Funiciello, Fabio Corbi

Elenora van Rijsingen, Serge Lallemand, Michel Peyret, Diane Arcay, Arnauld Heuret, et al.. How Subduction Interface Roughness Influences the Occurrence of Large Interplate Earthquakes. Geochemistry, Geophysics, Geosystems, 2018, 19 (8), pp.2342 - 2370. 10.1029/2018GC007618 . hal-01891873

Geochemistry, Geophysics, Geosystems

RESEARCH ARTICLE
10.1029/2018GC007618

How Subduction Interface Roughness Influences the Occurrence of Large Interplate Earthquakes

Elenora van Rijsingen[1,2], **Serge Lallemand**[1], **Michel Peyret**[1], **Diane Arcay**[1], **Arnauld Heuret**[3], **Francesca Funiciello**[2], **and Fabio Corbi**[2]

[1]Géosciences Montpellier, CNRS, Montpellier University, Montpellier, France, [2]Laboratory of Experimental Tectonics, Roma Tre University, Rome, Italy, [3]Géosciences Montpellier, Guyane University, Cayenne, France

Key Points:

- We present SubQuake: a new database containing spatial characteristics for 182 $M_W \geq 7.5$ subduction interplate earthquakes
- A global, quantitative comparison is performed with the seafloor roughness seaward of the trench
- $M_W \geq 7.5$ ruptures occurred preferentially on smooth subducting seafloor; this is especially clear for $M_W > 8.5$ events

Supporting Information:

- Supporting Information S1

Correspondence to:
E. van Rijsingen,
elenora.vanrijsingen@uniroma3.it

Citation:
van Rijsingen, E., Lallemand, S., Peyret, M., Arcay, D., Heuret, A., Funiciello, F., & Corbi, F. (2018). How subduction interface roughness influences the occurrence of large interplate earthquakes. *Geochemistry, Geophysics, Geosystems*, *19*, 2342–2370. https://doi.org/10.1029/2018GC007618

Received 16 APR 2018
Accepted 13 JUN 2018
Accepted article online 26 JUN 2018
Published online 9 AUG 2018

Abstract The role of seafloor roughness on the seismogenic behavior of subduction zones has been increasingly addressed over the past years, although their exact relationship remains unclear. Do subducting features like seamounts, fracture zones, or submarine ridges act as barriers, preventing ruptures from propagating, or do they initiate megathrust earthquakes instead? We address this question using a global approach, taking into account all oceanic subduction zones and a 117-year time window of megathrust earthquake recording. We first compile a global database, SubQuake, that provides the location of a rupture epicenter, the overall rupture area, and the region where the largest displacement occurs (the seismic asperity) for $M_W \geq 7.5$ subduction interplate earthquakes. With these data, we made a quantitative comparison with the seafloor roughness seaward of the trench, which is assumed to be a reasonable proxy for the subduction interface roughness. We compare the spatial occurrence of megathrust ruptures, seismic asperities, and epicenters, with two roughness parameters: the short-wavelength roughness R_{SW} (12–20 km) and the long-wavelength roughness R_{LW} (80–100 km). We observe that ruptures with $M_W \geq 7.5$ tend to occur preferentially on smooth subducting seafloor at long wavelengths, which is especially clear for the $M_W > 8.5$ events. At both short and long wavelengths, seismic asperities show a more amplified relation with smooth seafloor than rupture segments in general. For the epicenter correlation, we see a slight difference in roughness signal, which suggests that there might be a physical relationship between rupture nucleation and subduction interface roughness.

Plain Language Summary Subduction zones are regions on Earth where an oceanic plate dives below another plate. Earthquakes that occur along the contact between plates in such regions are among the largest and most destructive on Earth. To better understand where these large earthquakes are most likely to occur, we look at the effect of seafloor roughness. A rough seafloor is often characterized by many topographic features, such as seamounts or ridges, while a smooth seafloor is generally more flat. On a global scale, we compared the roughness of the incoming seafloor of the downgoing plate, with the occurrence of large earthquakes in each subduction zone. We find that the seafloor in front of large earthquakes is generally smoother than in areas where no large earthquakes have occurred. This is the clearest for very large earthquakes, with magnitudes larger than 8.5. Investigating which parameters play a role in the location of earthquakes helps us to understand where future earthquakes are more likely to occur.

1. Introduction

Over the past decades, large interplate earthquakes ($M_W \geq 7.5$) in subduction zones have received a great deal of attention from the scientific community. Their high magnitudes, sometimes even exceeding M_W 9, make them among the most destructive earthquakes on Earth. Therefore, unravelling the mechanism and both the spatial and temporal occurrence of large megathrust earthquakes is of great importance. Why do some subduction zones frequently host such events, while others remain silent for hundreds of years? Many subduction zone parameters have been proposed to explain this (e.g., Lallemand & Heuret, 2017). It has long been thought that young and fast subducting plates were more likely to host such large events (Ruff & Kanamori, 1980), but the recent $M_W > 9.0$ Sumatra (2004) and Tohoku (2011) events have changed this perspective (e.g., Stein & Okal, 2007, 2011).

Another parameter that has been proposed for several decades already is the amount of sediments filling the trench (Brizzi et al., 2018; Heuret et al., 2012; Ruff, 1989; Scholl et al., 2015). It is shown that subduction zones with large amounts of trench sediments positively correlate with the occurrence of great interplate earthquakes. This relates to another theory that developed over the years, suggesting a negative correlation between subduction interface roughness and megathrust earthquakes (Bassett & Watts, 2015; Das & Watts, 2009; Heuret et al., 2012; Kelleher & McCann, 1976; Kopp, 2013; Loveless et al., 2010; Sparkes et al., 2010; Wang & Bilek, 2014). Subduction interface roughness results from a combined effect of topographic features on the seafloor (e.g., seamounts, ridges, or plateaus), amount of sediments, and possible deformation processes occurring during subduction (e.g., tectonic erosion).

Numerous studies focus on the effect of topographic features on the occurrence of a single or several megathrust events. Some propose that subducting features like seamounts or fracture zones could act as asperities and therefore facilitate large ruptures (Bilek et al., 2003; Cloos, 1992; Landgrebe & Müller, 2015; Müller & Landgrebe, 2012; Scholz & Small, 1997), while others propose the opposite: subducting topographic highs acting as barriers to rupture propagation (Geersen et al., 2015; Henstock et al., 2016; Kodaira et al., 2000; Mochizuki et al., 2008; Robinson et al., 2006; Wang & Bilek, 2011). Due to the discrepancy among the possible interpretations, sometimes restricted to a specific region or feature, the scientific community so far has not reached a general consensus on the relationship between megathrust earthquakes and subduction interface roughness.

Among different factors like temperature (e.g., Gutscher & Peacock, 2003; Peacock & Hyndman, 1999) or fluids (e.g., Heise et al., 2017; Ranero et al., 2008; Saffer, 2017; Saffer & Tobin, 2011) that may play a role in tuning megathrust seismicity, here we focus on the potential role of subduction interface roughness on the occurrence of $M_W \geq 7.5$ events. We use a global approach, taking into account all oceanic subduction zones and a 117-year time window of megathrust earthquakes recording. By performing a quantitative comparison, we aim to provide a first-order relationship, while at the same time acknowledging that exceptions in specific regions may still exist.

This work follows up on a previous study by Lallemand et al. (2018), who provide a global database of seafloor roughness seaward of all oceanic subduction zones—SubRough—and who already made a first-order comparison with several parameters related to the state of stress in subduction zones. We extend this approach by first providing a global database—SubQuake—for subduction megathrust earthquakes, which will then be compared in a quantitative way to the seafloor roughness seaward of the trench.

The SubQuake database lists events that occurred since 1900, detailing spatial characteristics for 182 interplate earthquakes with moment magnitude of ≥7.5. Since most of these earthquakes rupture a relatively large portion of the subduction megathrust (i.e., 10^3–10^5 km^2; Allen & Hayes, 2017), it is not sufficient to only consider the location of a rupture's hypocenter. To better understand how the size and location of seismic ruptures relate to the subducting seafloor roughness, a more accurate description of the spatial characteristics of these ruptures is necessary. Rupture initiation, propagation direction, rupture arrest, and the location of the largest displacement (i.e., the seismic asperity; e.g., Lay & Kanamori, 1981; Wang & Bilek, 2014) are all characteristics whose spatial occurrence is still poorly understood. The SubQuake database compiles information on earthquake epicenters, rupture area contours, and if possible seismic asperity contours. The maximum possible timespan in terms of catalogue completeness (i.e., 1900–2017), and the global coverage of the database, makes it a useful tool for studying spatial rupture characteristics with respect to many subduction zone parameters, not necessarily limited to the seafloor roughness as presented in this study. The entire database is available online via subquake.gm.univ-montp2.fr.

In this paper, we first briefly present the recently compiled SubRough database (Lallemand et al., 2018). Next, we present how the earthquake data for the new SubQuake database have been collected and discretized into an earthquake grid for each subduction zone. Then, we discuss the procedures used for the quantitative comparison with the seafloor roughness, followed by the comparison results. Finally, we discuss our main findings by looking at how they relate to the results and concepts previously published.

2. Methodology

2.1. The Roughness Database

For the global comparison between seafloor roughness and the occurrence of subduction megathrust earthquakes, we use the SubRough database, a parameter database estimating the seafloor roughness seaward of

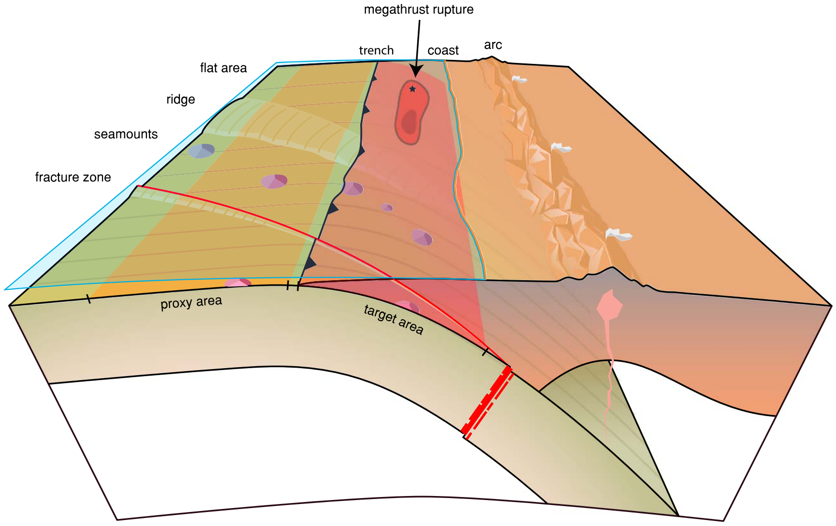

Figure 1. Overview of a subduction setting, indicating the area of the seafloor that is used as a proxy for the seismogenic zone (target area).

the trench, presented by Lallemand et al. (2018). They have developed an approach to estimate the roughness signal at different spatial wavelengths to characterize the seafloor bathymetry prior to subduction, to be used as a proxy for the roughness of the subduction interface (Figure 1).

From the General Bathymetric Charts of the Oceans database (Becker et al., 2009; Smith & Sandwell, 1997; Weatherall et al., 2015), the seafloor roughness has been determined by using power spectral densities. Over a 250-km-wide trench-parallel strip, a spectral analysis has been performed by using a circular sliding window (radius of 100 km; step of 10 km). Based on the resulting power spectral densities, two wavelength bandwidths have been selected for further analysis: a short-wavelength bandwidth from 12 to 20 km to compute one roughness parameter (R_{SW}) and a long-wavelength bandwidth from 80 to 100 km to compute the other parameter (R_{LW}). The choice for the R_{SW} bandwidth, the lower boundary, comes from the limited availability of high-resolution (i.e., $<$ 12 km) data in the General Bathymetric Charts of the Oceans data set. High-resolution measurements from ship surveys are only available for a few specific regions (i.e., only 10% of subduction trench length), while the lower resolution measurements from satellite gravity anomalies are available worldwide, with a global resolution of 12.5 km (Smith & Sandwell, 1997). The choice for the R_{LW} bandwidth, the upper boundary, is related to the size of the circular sliding window used for the spectral analysis. For wavelengths longer than 100 km, the number of samples within this window decreases, which makes power spectral density computations at very long wavelengths less reliable.

R_{SW} and R_{LW} highlight different topographic features on the seafloor, such as small- and intermediate-size seamounts and fracture zones in the short-wavelength roughness signals and large seamounts, seamount chains, and submarine ridges for long-wavelength roughness. Their respective roles in earthquake nucleation and rupture propagation/ending are likely to be very different, which may be tested by estimating their signature in the seafloor roughness separately. Roughness amplitudes at both wavelength bandwidths are given in meters, where 95% of the R_{SW} values generally fall within the [0–300 m] range, with a mean of 145 m. For R_{LW}, 95% of the roughness values vary in the range [0–1,500 m], with a mean around 485 m.

Both the short- and long-wavelength roughness parameters are used in this study, to perform a global and quantitative comparison between the seafloor roughness seaward of the trench and the occurrence of subduction megathrust earthquakes.

2.2. The SubQuake Database

One of the biggest challenges of compiling an earthquake database covering more than 100 years relies on the availability of the data and the disparity in quality. Because of the lack of good global and continuous

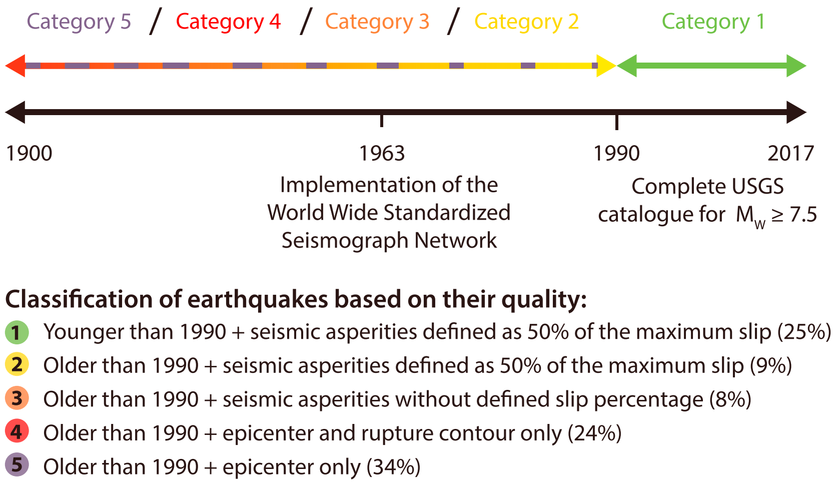

Figure 2. Categories of the SubQuake database. The classification is based on the age and seismic asperity definition of the event. For some events, no rupture contour data have been found, indicated by the dashed purple line (category 5). Percentage of ruptures related to the total number of events in the database is given for each category.

coverage of seismometers during most of the twentieth century, data are sparse and difficult to retrieve. In addition, the methods for obtaining slip distributions have improved considerably over the past decades, leading to more detailed solutions for recent events, often based on a combination of high quality seismic, geodetic, and/or tsunami data (e.g., Nocquet et al., 2016; Yue & Lay, 2013). In this section, we first address the already available databases that provide rupture slip distributions. Then, we discuss how we derived the earthquake's epicenters, rupture contours, and seismic asperity contours and how we accounted for the difference in quality. Finally, we explain how the data have been discretized into a rupture grid covering all subduction zones.

2.2.1. Already Available Databases

Several attempts have been made to compile a database providing information on the spatial characteristics of seismic ruptures, not in particular dedicated to subduction megathrust earthquakes (Hayes, 2017; Mai & Thingbaijam, 2014; Ye et al., 2016). The SRCMOD database displays 364 finite fault rupture models for 169 earthquakes over a time frame of ~100 years. This database shows different models for the same event and displays the various methods that have been used to obtain slip distributions. Recent events are very well represented (e.g., 21 different inversion models for the 2011 Tohoku earthquake; Lay, 2017), while only very few inversion models exist for events older than 1960. Ye et al. (2016) and Hayes (2017; USGS) also gathered rupture models for different events but chose a specific time window (1990–present) and a consistent modeling approach. Ye et al. (2016) documented finite fault models for all $M_W \geq 7.0$ subduction interplate earthquakes from 1990 to 2015, based on global broadband body wave inversions. Hayes (2017) used finite fault models based on body- and surface-wave solutions (Ji et al., 2002) and provides a complete catalogue for ruptures with $M_W \geq 7.5$ since 1990 (further referred to as the USGS database). The latter two approaches lead to a more homogeneous database, in which different events can be compared more reliably.

2.2.2. SubQuake Data Compilation and Classification

For compiling the SubQuake database, hypocenters of $M_W \geq 7.5$ events from the recently updated ISC-GEM catalogue (Storchak et al., 2013, updated in January 2016) were analyzed to select subduction megathrust earthquakes. The selection criteria for this analysis follow from Heuret et al. (2011), which include examining the focal mechanism, hypocenter depth, fault plane orientation, and distance from the trench. If no information about the nature of the event could be found (in the case of events older than 1975), the earthquake is assumed to be a thrusting event along the subduction plate interface because of its large magnitude.

For collecting earthquake rupture contours, we rely on the SRCMOD and USGS databases, as well as on many individual publications. Before the implementation of the World Wide Standardized Seismograph Network in 1963, earthquake rupture zones were mainly determined by using aftershocks. The older publications we use in this study therefore usually provide only an estimate of the rupture area. When seismic data became more abundant, people started using strong ground motions and teleseismic data to calculate slip distributions

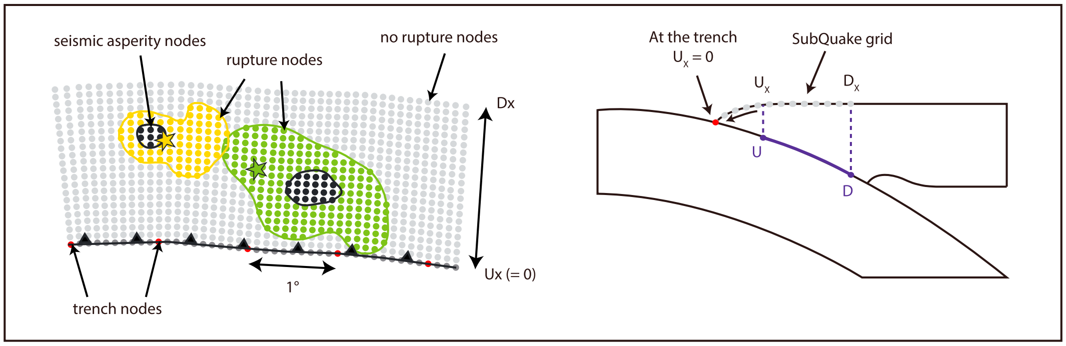

Figure 3. SubQuake data discretization. Trench nodes have been interpolated every 0.1° and projected in a trench-perpendicular direction, delimited by U_x and D_x, the horizontal distances to the trench from the updip (U) and the downdip limit (D) of the seismogenic zone, respectively. After reviewing the trenchward extent of the SubQuake ruptures, U_X has been set to 0. Nodes falling within a rupture or seismic asperity contour are classified as rupture (colored according to Figure 2 categories) and seismic asperity nodes (black). Stars depict epicenters. All remaining nodes are classified as no-rupture nodes (grey).

(e.g., Beck & Ruff, 1987). This not only allowed them to determine the spatial extent of the rupture area but also gave them more insights in rupture evolution (e.g., the 1986 M_W 8.0 Andreanof Islands earthquake; Das & Kostrov, 1990). Over the past decades, seismic inversion techniques have improved significantly, resulting in an increase in the accuracy of rupture characteristics. In addition, the ongoing development of continuous GPS measurements and InSAR data contributes to a better determination of co-seismic slip but also allows to better monitor the coupling during the interseismic phase within subduction zones (e.g., Métois et al., 2012). However, all these new technologies and improved methods result in many different inversion models for the same seismic event, often showing different slip distribution solutions.

We therefore chose to use the USGS database as a basis for the most recent events (i.e., ≥1990) in order to keep the inversion method as consistent as possible. Several exceptions exist, for which we believe that another inversion model yields a more accurate representation of the slip distribution, thanks to a combination of high quality seismic and geodetic data (e.g., Sumatra 2004, Tohoku 2011, and Pedernales 2016). For events older than 1990, we either relied on the SRCMOD database or on individual publications, in which we selected rupture models as a function of the methods that were implemented. In addition, we integrated information from Bassett and Watts (2015), who collected many rupture contours for several major subduction zones.

From the studies providing information on the slip distribution, we extracted seismic asperity regions. For the digital slip distributions provided by the USGS and SRCMOD databases, we defined seismic asperities as regions exceeding "50% of the maximum slip," following the definition by Yamanaka and Kikuchi (2004). For the remaining events, we relied on the seismic asperity information given by individual studies.

All events in the SubQuake database are classified as a function of their quality (Figure 2). We chose to use a classification system based on the rupture age and the way its seismic asperity is defined. The age and determination method of the seismic asperity in a study adequately reflect the quality of the model, both in terms of event age and method used (e.g., old rupture models based on aftershock distributions cannot indicate a seismic asperity and therefore belong to category four). Ruptures for which we were not able to obtain any information about the rupture contour have been classified as category 5.

2.2.3. Assembling the SubQuake Data into a Grid

The SubQuake data are assembled into a grid for all subduction zones (Figure 3). This grid is a surface projection of the seismogenic zone, for which the trench-perpendicular extent is based on Heuret et al. (2011), who defined the horizontal distance from the trench to the updip and the downdip limits of the seismogenic zone for all subduction zones (U_x and D_x, respectively). The node spacing (10 km) is chosen to be the same as the one of the SubRough grid. The SubQuake rupture and seismic asperity contours are used to assign each grid node with a specific seismic behavior, either "no rupture," "rupture" (taking into account the four different rupture categories), or "seismic asperity." More detailed information about the compilation of the SubQuake grid can be found in the supporting information (section S1).

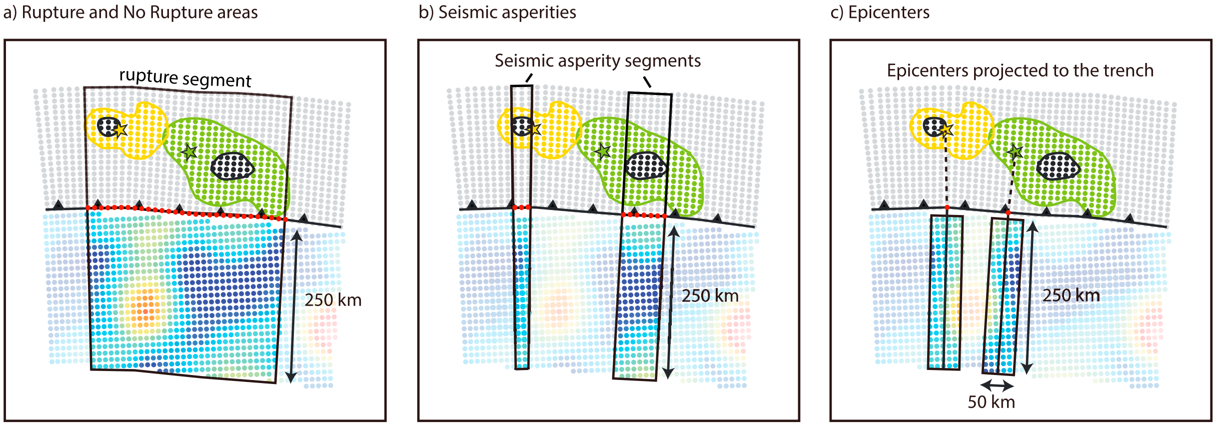

Figure 4. Trench segmentation and data selection as a function of seismogenic behavior: rupture and seismic asperity (a and b) and epicenters (c). Colors in the SubQuake grid (landward of the trench) represent the rupture categories (see Figure 2); colors on the seaward side illustrate the variety of seafloor roughness (from dark blue being smooth to red being rough). Red nodes depict the along trench segments, and stars depict epicenters.

2.3. Comparison strategy

A global, quantitative comparison between the SubRough and SubQuake data sets is done following two strategies: the first one is based on the SubQuake grid (for rupture and seismic asperity contours), while the second one focuses on the location of rupture epicenters. The aim of these comparison strategies is to evaluate the presence of a rupture, seismic asperity, or epicenter in the SubQuake grid and subsequently select the roughness data that face these regions seaward of the trench. Both procedures will briefly be discussed below. More detailed descriptions of the comparison algorithms can be found in the supporting information (section S2).

2.3.1. SubQuake Grid and Facing SubRough Data

The 2D SubQuake grid has been divided into 1D segments along the trench, based on the occurrence of ruptures and seismic asperities. An algorithm evaluates the presence of either rupture or seismic asperity nodes in the continuation of every trench node, following the trench-perpendicular azimuth (Figures 4a and 4b). This results in a selection of trench segments for all three categories (i.e., no rupture, rupture, and seismic asperity). Note that the no-rupture segments simply indicate regions where no $M_W \geq 7.5$ have been observed between 1900 and 2017. They should not be directly interpreted as areas where ruptures can never occur, since the recurrence time may exceed the 117-year time window due to low subduction rates or only partial coupling.

With this segment approach, the trench-perpendicular information of the SubQuake grid is lost, since the algorithm does not take into account the number of rupture or seismic asperity nodes found in the continuation of each trench node. However, since we use the roughness seaward of the trench as a proxy for the subduction interface, our knowledge of trench-perpendicular roughness variations is limited. We therefore mainly focus on the trench-parallel variations in subduction interface roughness.

Based on the three different types of segments, the SubRough data seaward of the trench, for both the short-wavelength R_{SW} and the long-wavelength R_{LW}, can be selected and evaluated (see section 2.1 for details). For this, we use a trench-perpendicular direction for data selection, except for some regions where we take into account the obliquity of specific linear features extending into the trench (i.e., for the Joban Seamount chain in Japan, the Louisville ridge in Tonga, and the Murray Ridge in Makran). In most cases, the seafloor right in front of the trench is a good proxy for the subduction interface (Bassett & Watts, 2015; S. Das & Watts, 2009), and the use of this proxy therefore seems a reasonable assumption for this global study. The roughness data selected for the rupture, no-rupture, and seismic asperity segment groups are analyzed in terms of density distribution, illustrating which roughness amplitudes are the most common.

2.3.2. Epicenters and Facing SubRough Data

All 182 epicenters have been correlated with R_{SW} and R_{LW} seaward of the trench. For each epicenter, the closest trench node has been selected based on a spherical approximation with great circles (Global Mapping Tools, Wessel et al., 2013). For these trench nodes, roughness data perpendicular to the trench are selected within a 50-km-wide and 250-km-long strip (i.e., taking into account the complete width of the roughness bands; Figure 4c). For epicenters located in regions where an oblique projection has been performed for the SubQuake grid, the same modified azimuth has been used for roughness data selection.

3. Results

The results of this study are presented in two main sections: (1) the new global database that we compiled and (2) the comparison with the seafloor roughness data. Regarding the SubQuake database (section 3.1), we discuss the location of a rupture's epicenter with respect to its seismic asperity (section 3.1.1.), and we classify all subduction zones according to their rupture length ratio (section 3.1.2). In section 3.2, where we show the comparison to the seafloor roughness, we first discuss a first-order comparison between the rupture length ratio and the percentage of smooth seafloor for each region. Then we discuss in more detail nine regions that together represent the variety of observed seismogenic behavior, after which we study the relation between earthquake magnitude and seafloor roughness at a global scale. Finally, we show the comparison of seismic asperity segments and rupture epicenters to the seafloor roughness.

3.1. SubQuake Results

Table 1 lists all $M_W \geq 7.5$ subduction megathrust earthquakes since. From the 82 collected ruptures in our database, 45 events are category 1 ruptures, 16 category 2, 15 category 3, 44 category 4, and 62 for category 5. In the supporting information, the relationship between rupture area and moment magnitude for categories 1–4 is described and compared to several existing scaling relationships (Allen & Hayes, 2017; Strasser et al., 2010).

3.1.1. Epicenter Location With Respect to Seismic Asperity

With the seismic asperity and epicenter data, we can evaluate how often the location of a rupture's epicenter is overlapping with the area of maximum slip. We observe that for 47% of category 1 events, the epicenter is located within the seismic asperity contour. When also considering categories 2 and 3, for which the uncertainty in both epicenter and seismic asperity location is higher, we observe that 37% of epicenters are located within the seismic asperity.

3.1.2. Subduction Zone Classification in Terms of Rupture Length Ratio

In Table 2, the subduction zones considered in this study have been ordered in terms of rupture length ratio (RLR). Rupture percentages have been calculated based on the trench-parallel length of the rupture segments in relation to the total trench length. Since we do not take into account the category 5 ruptures when calculating this ratio, it should be seen as a minimum RLR. We defined four different classes based on the occurrence of $M_W \geq 7.5$ ruptures: high RLR (with $>75\%$ of the trench length covered by ruptures), intermediate rupture length ratio ($25\% < \text{RLR} < 75\%$), low RLR (with $\text{RLR} < 25\%$), and finally the regions where no cat. 1–4 $M_W \geq 7.5$ ruptures have been observed. Regions that fall in the "high RLR" class are Japan-Kuril-Kamchatka, South Andes, Alaska-Aleutian, and Andaman-Sumatra. The regions in the "intermediate RLR" class are North Andes, Central America, New-Guinea-Solomon-Vanuatu, Ryukyu-Nankai, and Makran, in order of decreasing rupture length ratio. The regions with low RLR are Java-Sumba, Tonga-Kermadec, the Antilles, and the Philippines. Both the Antilles and the Philippines, but also the Makran subduction zone in the "intermediate RLR" class, only contain one or two category 4 ruptures; all older than 1975. The four regions that did not host any category 1–4 $M_W \geq 7.5$ ruptures between 1900 and 2017 are Cascadia, Izu-Bonin-Mariana, Luzon, and South Sandwich.

3.2. Comparison Between SubRough and SubQuake

3.2.1. Rupture Length Ratio Versus Percentage of Smooth Seafloor

Following the classification of subduction zones based on their RLR (Table 2), we calculated the percentage of smooth seafloor for each region to make a first-order comparison with the RLR. Lallemand et al. (2018) used thresholds of 250 and 1,000 m to identify whether an area can be considered dominantly smooth, mixed, or dominantly rough (at long wavelengths, R_{LW}). We followed the 250 m threshold to determine the percentages of smooth seafloor for each region, which are indicated in Table 2. When plotting the relationship between RLR and smooth seafloor (Figure 5), we clearly observe that regions with smoother seafloor also have higher RLR. We can distinguish two groups: the regions with $\text{RLR} > 50\%$, which all show large percentages of smooth seafloor, and the regions with $\text{RLR} < 50\%$, which show a more mixed signal in terms of smooth seafloor. We highlighted two outliers in Figure 5: the New-Guinea-Solomon-Vanuatu and Cascadia subduction zones, which both do not fit the general trend that we observe.

Table 1
List of All SubQuake Events

No.	Location	Date	M_W	Cat	Method	Author
182	Puerto Quellon, Chile	25 December 2016	7.61	1	Body/Surf	Hayes (2017)
181	Pedernales, Ecuador	16 April 2016	7.82	1	Body/HRGPS/InSAR	Nocquet et al. (2016)
180	Illapel, Chile	16 September 2015	8.23	1	Body/Surf	Hayes (2017)
179	Kokopo, Papua New Guina	5 May 2015	7.47	1	Body/Surf	Hayes (2017)
178	Panguna, Papua New Guinea	19 April 2014	7.47	1	Body/Surf	Hayes (2017)
177	Iquique, Chile	3 April 2014	7.78	1	Body/Surf	Hayes (2017)
176	Iquique, Chile	1 April 2014	8.18	1	Body/Surf	Hayes (2017)
175	Costa Rica	5 September 2012	7.62	1	Body/Surf	Hayes (2017)
174	Oaxaca, Mexico	20 March 2012	7.47	1	Body/Surf	Hayes (2017)
173	Tohoku, Japan	11 March 2011	9.09	1	Body/Surf/HRGPS	Yue and Lay (2013)
172	Kepulauan Mentawai, Indonesia	25 October 2010	7.83	1	Body/Surf	Hayes, 2017
171	Northern Sumatra	6 April 2010	7.82	1	Body/Surf	Hayes, 2017
170	Maule, Chile	27 February 2010	8.79	1	Body/Surf	Hayes, 2017
169	Vanuatu	7 October 2009	7.62	1	Body/Surf	Hayes, 2017
168	Antofagasta, Chile	14 November 2007	7.73	1	Body/Surf	Hayes, 2017
167	Sumatra, Indonesia	12 September 2007	8.49	1	Body/Surf	Hayes, 2017
166	Pisco, Peru	15 August 2007	7.97	1	Body/Surf	Hayes, 2017
165	Solomon Islands	1 April 2007	8.07	1	Body/Surf	Hayes, 2017
164	Kuril Islands	15 November 2006	8.3	1	Body/Surf	Hayes, 2017
163	Java, Indonesia	17 July 2006	7.72	1	Body/Surf	Hayes, 2017
162	Tonga	3 May 2006	7.97	1	Body/Surf	Hayes, 2017
161	Sumatra, Indonesia	28 March 2005	8.62	1	Body/Surf	Hayes, 2017
160	Sumatra, Indonesia	26 December 2004	9.00	1	Body/Surf	Ammon et al. (2005)
159	Rat Islands, Alaska	17 November 2003	7.76	1	Body/Surf	Hayes (2017)
158	Hokkaido, Japan	25 September 2003	8.26	1	Body/Surf	Hayes (2017)
157	Colima, Mexico	22 January 2003	7.48	1	Body/Surf	Hayes (2017)
156	Southern Peru	7 July 2001	7.61	1	Body/Surf	Hayes (2017)
155	Southern Peru	23 June 2001	8.39	1	Body/Surf	Hayes (2017)
154	New Britain, Papua New Guinea	17 November 2000	7.77	1	Body/Surf	Hayes (2017)
153	New Ireland, Papua new Guinea	16 November 2000	7.81	1	Body/Surf	Hayes (2017)
152	Kamchatka	5 December 1997	7.76	1	Body/Surf	Hayes (2017)
151	Santa Cruz Islands	21 April 1997	7.70	1	Body/Surf	Hayes (2017)
150	Central Peru	12 November 1996	7.71	1	Body/Surf	Hayes (2017)
149	Andreanof Islands	10 June 1996	7.88	1	Body/Surf	Hayes (2017)
148	Northern Peru	21 February 1996	7.51	1	Body/Surf	Hayes (2017)
147	Kuril Islands	3 December 1995	7.88	1	Body/Surf	Hayes (2017)
146	Colima, Mexico	9 October 1995	7.98	1	Body/Surf	Hayes (2017)
145	Bougainville, Papua New Guinea	16 August 1995	7.72	1	Body/Surf	Hayes (2017)
144	Antofagasta, Chile	30 July 1995	8.00	1	Body/Surf	Hayes (2017)
143	Honshu, Japan	28 December 1994	7.73	1	Body/Surf	Hayes (2017)
142	Java, Indonesia	2 June 1994	7.76	1	Body/Surf	Hayes (2017)
141	Kamchatka	8 June 1993	7.48	1	Body/Surf	Hayes (2017)
140	Nicaragua	2 September 1992	7.63	1	Body/Surf	Hayes (2017)
139	Kuril Islands	22 December 1991	7.57	1	Body/Surf	Hayes (2017)
138	Costa Rica	22 April 1991	7.62	1	Body/Surf	Hayes (2017)
137	Mindanao, Philippines	15 December 1989	7.52	5	—	
136	Antofagasta, Chile	5 March 1987	7.54	5	—	
135	Andreanof Islands	7 May 1986	7.95	3	Body	Boyd et al. (1995)
134	Guerrero, Mexico	21 September 1985	7.54	3	Body	Ruff and Miller (1994)
133	Michoacan, Mexico	19 September 1985	7.97	2	Body/SGM	Mendoza and Hartzell (1989)
132	Valparaiso, Chile	3 March 1985	7.95	2	Body/Surf/SGM	Mendoza et al. (1994)
131	Solomon Islands	7 February 1984	7.54	5	—	
130	Atacama, Chile	4 October 1983	7.63	5	—	
129	Costa Rica	3 April 1983	7.45	3	Body/Surf	Adamek et al. (1987)
128	Tonga	19 December 1982	7.47	4	Aftershocks	Christensen and Lay (1988)
127	Loyalty Islands	25 October 1980	7.45	4	Aftershocks	Tajima and Kanamori (1985)
126	Santa Cruz Islands	17 July 1980	7.73	5	—	Tajima and Kanamori (1985)
125	Santa Cruz Islands	8 July 1980	7.47	5	—	Tajima and Kanamori (1985)
124	Ecuador	12 December 1979	8.09	3	Body/Surf	Swenson and Beck (1996)

Table 1 *(continued)*

No.	Location	Date	M_W	Cat	Method	Author
123	Oaxaca, Mexico	29 November 1978	7.75	4	Aftershocks	Singh et al. (1985)
122	Honshu, Japan	12 June 1978	7.63	2	SGM	Yamanaka and Kikuchi (2004)
121	Kuril Islands	23 March 1978	7.56	4	Aftershocks	Perez (2000)
120	Kermadec Islands	14 January 1976	7.79	4	Aftershocks	Nishenko (1991)
119	Tonga, Samoa Islands	26 December 1975	7.70	5	—	Tajima and Kanamori (1985)
118	Philippines	31 October 1975	7.50	5	—	
117	Solomon Islands, doublet (a)	20 July 1975	7.60	4	Body/Surf	Lay and Kanamori (1980)
116	Solomon Islands, doublet (b)	20 July 1975	7.60	4	Body/Surf	Lay and Kanamori (1980)
115	Kuril Islands	10 June 1975	7.50	4	Aftershocks	Schwartz and Ruff (1987)
114	Central Peru	3 October 1974	8.10	2	Body	Hartzell and Langer (1993)
113	Hokkaido, Japan	17 June 1973	7.80	3	Body	Schwartz and Ruff (1987)
112	Kuril Islands	28 February 1973	7.50	5	—	
111	Colima, Mexico	30 January 1973	7.60	3	Body	Ruff and Miller (1994)
110	Mindanao, Philippines	2 December 1972	8.00	4	Aftershocks	Acharya (1980)
109	Solomon Islands	17 August 1972	7.50	5	—	
108	Solomon Islands	26 July 1971	8.10	2	Body	Park and Mori (2007)
107	Solomon Islands	14 July 1971	8.00	2	Body	Park and Mori (2007)
106	Valparaiso, Chile	9 July 1971	7.80	4	Aftershocks	Comte et al. (1986)
105	Sumatra	21 November 1969	7.59	5	—	Tajima and Kanamori (1985)
104	Kuril Islands	11 August 1969	8.20	3	Body	Schwartz and Ruff (1985)
103	Talaud, East Indonesia	30 January 1969	7.60	5	—	
102	Honshu, Japan	16 May 1968	8.20	2	Body, SGM, other	Nagai et al. (2001)
101	Nankai	1 April 1968	7.50	5	Aftershocks	Wyss (1976)
100	Santa Cruz Islands	31 December 1966	7.80	4	Aftershocks	Kelleher et al. (1974)
99	Antofagasta, Chile	28 December 1966	7.70	4	Unknown	Kelleher (1972)
98	Central Peru	17 October 1966	8.10	3	Body	Beck and Ruff (1989)
97	Vanuatu	11 August 1965	7.60	4	Aftershocks	Kelleher et al. (1974)
96	Fox Islands, Alaska	2 July 1965	7.80	4	Aftershocks	Sykes (1971)
95	Rat Islands, Alaska	4 February 1965	8.70	3	Body	Beck and Christensen (1991)
94	Puysegur	12 September 1964	7.60	5	—	
93	Alaska	28 March 1964	9.30	2	Level/Tsunami/Tri/Sea	Holdahl and Sauber (1994)
92	Kuril Islands	13 October 1963	8.50	3	Body	Beck and Ruff (1987)
91	Kyushu, Japan	26 February 1961	7.54	4	Aftershocks	Wyss (1976)
90	Central Peru	20 November 1960	7.60	5	—	Pelayo and Wiens (1990)
89	Bio-Bio, Chile	22 May 1960	9.60	2	Level/Sea	Barrientos and Ward (1990)
88	Honshu, Japan	20 March 1960	7.95	2	SGM	Yamanaka and Kikuchi (2004)
87	Kamchatka	4 May 1959	7.90	4	Unknown	Fedotov et al. (2011)
86	Kuril Islands	6 November 1958	8.40	3	Body	Schwartz and Ruff (1987)
85	Ecuador	19 January 1958	7.60	3	Body	Swenson and Beck (1996)
84	Guerrero, Mexico	28 July 1957	7.60	4	Body	Beroza et al. (1984)
83	Aleutian Islands, Alaska	9 March 1957	8.60	2	Body/Surf/Tsunami	Johnson et al. (1994)
82	Japan (Honshu)	29 September 1956	7.53	5	—	
81	Kermadec	27 February 1955	7.52	5	—	
80	Honshu, Japan	25 November 1953	7.90	4	Tsunami	Matsuda et al. (1978)
79	Chile	6 May 1953	7.55	5	—	
78	Kamchatka	4 November 1952	8.90	2	Tsunami	Johnson and Satake (1999)
77	Hokkaido, Japan	4 March 1952	8.10	2	Tsunami	Hirata et al. (2003)
76	Vanuatu	2 December 1950	7.90	5	—	Kelleher et al. (1974)
75	Tonga	8 September 1948	7.50	5	—	Okal et al. (2004)
74	Nankaido, Japan	20 December 1946	8.30	2	Tsunami	Baba et al. (2002)
73	New Ireland, Papua new Guinea	29 September 1946	7.68	5	—	
72	Domenican Republic	4 August 1946	7.76	4	Aftershocks	Kelleher et al. (1973)
71	British Columbia	23 June 1946	7.50	5	—	
70	Alaska	1 April 1946	8.60	4	Unknown	Sykes (1971)
69	New Britain	28 December 1945	7.50	5	—	
68	Pakistan	27 November 1945	8.10	4	Body, Level	Byrne et al. (1992)
67	Puysegur	1 September 1945	7.50	5	—	
66	Tonankai, Japan	7 December 1944	8.10	2	Tsunami	Tanioka and Satake (2001)
65	Puerto Rico	29 July 1943	7.70	4	Aftershocks	Kelleher et al. (1973)
64	Philippines	25 May 1943	7.76	5	—	Acharya (1980)

Table 1 *(continued)*

No.	Location	Date	M_W	Cat	Method	Author
63	Coquimbo, Chile	6 April 1943	8.10	3	Body	Beck et al. (1998)
62	Central Peru	24 August 1942	8.10	4	Body	Swenson and Beck (1996)
61	Guatemala	6 August 1942	7.70	4	Aftershocks	Kelleher et al. (1973)
60	Ecuador	14 May 1942	7.80	3	Aftershocks	Swenson and Beck (1996)
59	Costa Rica	5 December 1941	7.52	4	Aftershocks	Kelleher et al. (1973)
58	Nankai	18 November 1941	8.02	5	—	
57	Andaman Islands	26 June 1941	7.60	4	Aftershocks	Bilham et al. (2005)
56	Michoacan, Mexico	15 April 1941	7.60	4	Aftershocks	Kelleher et al. (1973)
55	Mariana	28 December 1940	7.70	5	—	Okal (2012)
54	Central Peru	24 May 1940	8.20	4	Body	Beck and Ruff (1989)
53	Nicoya, Costa Rica	21 December 1939	7.59	4	Aftershocks	Kelleher et al. (1973)
52	Solomon Islands	30 April 1939	7.95	5	—	
51	Solomon Islands	30 January 1939	7.82	5	—	
50	Alaska	10 November 1938	8.30	2	Tsunami	Johnson and Satake (1994)
49	Fukushima-Oki, Japan (1)	5 November 1938	7.80	4	Tsunami	Hashimoto et al. (2009)
48	Fukushima-Oki, Japan (2)	5 November 1938	7.70	4	Tsunami	Hashimoto et al. (2009)
47	Ryukyu	16 June 1938	7.60	5	—	
46	Ryukyu	10 June 1938	7.66	5	—	
45	Japan (Fukushima-Oki)	23 May 1938	7.70	5	—	Hashimoto et al. (2009)
44	Chile	13 July 1936	7.52	5	—	
43	Philippines	1 April 1936	7.75	5	—	Acharya (1980)
42	Kepulauan Batu, Indonesia	28 December 1935	7.60	4	Body	Rivera et al. (2002)
41	Solomon Islands	15 December 1935	7.60	5	—	
40	Santa Cruz Islands	18 July 1934	7.70	4	Aftershocks	Kelleher et al. (1974)
39	Mariana	24 February 1934	7.50	5	—	
38	Manila trench	14 February 1934	7.50	5	—	Duong et al. (2009)
37	Sumatra	24 June 1933	7.53	5	—	
36	Colima, Mexico	18 June 1932	7.80	4	Aftershocks	Pacheco et al. (1997)
35	Nankai	2 November 1931	7.93	5	—	
34	Solomon Islands	10 October 1931	7.95	5	—	
33	Solomon Islands	3 October 1931	7.88	5	—	
32	Honshu, Japan	9 March 1931	7.98	4	SGM	Yamanaka and Kikuchi (2004)
31	Japan	10 November 1930	7.73	5	—	
30	Maule, Chile	1 December 1928	7.70	4	Aftershocks	Beck et al. (1998); Bilek (2010)
29	Oaxaca, Mexico	22 March 1928	7.73	4	Aftershocks	Kelleher et al. (1973)
28	Vanuatu	16 March 1928	7.53	5	—	Kelleher et al. (1974)
27	Kamchatka	3 February 1923	8.40	4	Aftershocks	Johnson and Satake (1999)
26	Atacama, Chile	11 November 1922	8.30	3	Aftershocks	Beck et al. (1998)
25	Taiwan	1 September 1922	7.59	5	—	Theunissen et al. (2012)
24	Vanuatu	20 September 1920	8.15	5	—	
23	Taiwan	5 June 1920	8.23	4	Other	Theunissen et al. (2010)
22	New Britain/Solomon Islands	2 February 1920	7.81	5	—	
21	New Britain/Solomon Islands	6 May 1919	7.75	5	—	
20	Tonga	30 April 1919	8.10	5	—	Okal et al. (2004)
19	Chile	4 December 1918	7.83	5	—	
18	Kuril Islands	8 November 1918	7.79	4	Unknown	Fedotov et al. (2011)
17	Kermadec	1 May 1917	8.20	5	—	
16	Solomon Islands	1 January 1916	7.89	5	—	
15	Kuril Islands	1 May 1915	7.80	5	—	
14	Southern Sumatra	25 June 1914	7.57	4	Unknown	Natawidjaja et al. (2004)
13	Southern Peru	6 August 1913	7.74	4	Unknown	Kelleher (1972)
12	Tonga	26 June 1913	7.74	5	—	
11	Philippines	14 March 1913	7.77	5	—	
10	Mexico	7 June 1911	7.60	5	—	
9	Philippines	16 December 1910	7.61	5	—	
8	Guerrero, Mexico	30 July 1909	7.50	5	—	
7	Mexico	15 April 1907	7.80	5	—	
6	Northern Sumatra	4 January 1907	7.80	5	Other	Newcomb and McCann (1987)
5	Valparaiso, Chile	17 August 1906	8.20	4	Unknown	Bilek (2010)
4	Ecuador	31 January 1906	8.35	4	Unknown	Kelleher (19720

Table 1 *(continued)*

No.	Location	Date	M_W	Cat	Method	Author
3	Kamchatka	25 June 1904	7.70	5	Unknown	Fedotov et al. (2011)
2	Mexico	14 January 1903	7.69	5	—	
1	Vanuatu	9 August 1901	7.92	5	—	

Note. Methods: Body = body waves, Surf = surface waves, SGR = strong ground motion, GPS = Global Positioning System, HRGPS = high rate GPS, InSAR = interferometric synthetic-aperture radar, Tsunami = tide gauge data, Level = leveling data based on coseismic elevation changes, Tri = triangulation data based on horizontal co-seismic displacements, Sea = data based on sea-level changes, Aftershocks = spatial distribution of smaller earthquakes that occurs in the same area, after the mainshock.

3.2.2. Rupture Areas: Specific Regions

By qualitatively comparing the SubQuake grid on the landward side of the trench and the SubRough data on the seaward side, some areas already suggest a possible relationship between the roughness of the seafloor and the occurrence of megathrust earthquakes. Figures 6 and 7 show the SubQuake grids for the six subduction zones where the rupture length ratio is the highest, as well as three regions representative for the remaining groups of Table 2. Seaward of the trenches, the SubRough data at both wavelength bandwidths (i.e., R_{SW} and R_{LW}) are plotted. Individual figures for all subduction zones in Table 2 can be found in Figures S2 to S16 in the supporting information. As can be seen in Figure 7, all the subduction zones with RLR $>$ 50% face mainly smooth to moderately rough seafloor, as shown in Figure 5 and demonstrated as well by Lallemand et al. (2018).

Figure 8 shows density distributions for the long-wavelength roughness signal of the subduction zones displayed in Figures 6 and 7, illustrating which roughness amplitudes are the most common for these regions. Density has been multiplied by the number of grid points in each data set (i.e., rupture or no-rupture groups for each region) to obtain the count, which better highlights the size of the different groups. Density plots for the remaining regions can be found in the supporting information (Figure S17). The comparison between seaward roughness and interface seismicity for the subduction zones displayed in Figures 7 and 8 will be briefly discussed below, both qualitatively and quantitatively. Since the regions with

Table 2
Subduction Zone Classification according to Rupture Length Ratio

Class	Region	Rupture length ratio RLR (%)	Percentage of $R_{LW} < 250$ m (%)
High rupture length ratio (>75%)	**Japan-Kuril-Kamchatka**	96	52
	South Andes	93	67
	Alaska-Aleutian	89	69
	Andaman-Sumatra	79	53
Intermediate rupture length ratio (>25% and <75%)	**North Andes**	58	51
	Central America	53	56
	New Guinea-Solomon-Vanuatu	46	4
	Ryukyu-Nankai	29	16
	Makran	27	22
Low rupture length ratio (<25%)	**Java-Sumba**	18	23
	Tonga-Kermadec	14	41
	Antilles	11	49
	Philippines	10	27
No $M_W \geq 7.5$ ruptures[a]	**Cascadia**	0	78
	Izu-Bonin-Mariana	0	19
	Luzon	0	42
	South Sandwich	0	54

Note. Percentages of trench length that has hosted ruptures have been calculated and organized into four categories. Percentages of long-wavelength roughness (R_{LW}) with amplitudes below 250 m are indicated for region as well. Regions indicated in bold are displayed in Figures 6, 7, and 8.
[a] Except for several category 5 events, for which it is uncertain whether they are interplate events.

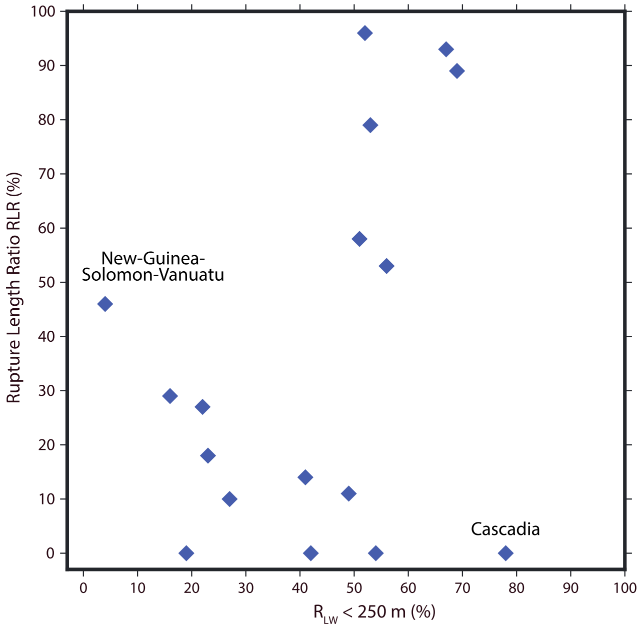

Figure 5. Rupture length ratio (RLR) versus percentage of smooth seafloor ($R_{LW} < 250$ m). Blue diamonds all represent one region from Table 2. Two outliers, New-Guinea-Solomon-Vanuatu and Cascadia, are indicated.

very high RLR display large differences in counts between rupture and no-rupture segments, a quantitative comparison for these specific zones is difficult. The same holds for the Java-Sumba region, where the count for the rupture segments is rather low with respect to the no-rupture segments.

3.2.2.1. Japan-Kuril-Kamchatka

The Japan-Kuril-Kamchatka trench has the largest rupture length ratio; 96% of the forearc has ruptured. This area is among the smoother ones, except at the two edges of the region. In the north, the subducting Emperor Seamount Chain is clearly visible in the roughness signal. This also holds for the Joban Seamount Chain in the south, offshore Japan. This chain intersects the Japan Trench with an angle of roughly 55° (measured from north) and is assumed to continue with this trend into the subduction zone (e.g., Bassett & Watts, 2015; Nishizawa et al., 2009). The partly subducted Daiichi-Kashima seamount (Lallemand et al., 1989), and another large seamount along the plate interface (Mochizuki et al., 2008), supports this assumption. When looking at the SubQuake data on the landward side of the trench, no rupture has recently occurred at the location where the Joban Seamount chain is subducting, while the Tohoku 2011 rupture (no. 173 in Figure 7) and the two 1938 ruptures (nos. 48 and 49) all stop where the Joban Seamount chain enters the subduction zone. Another rupture, from 1953 (no. 80), has occurred south of the Joban Seamount chain, where the seafloor roughness becomes smoother again (following the 55° extrapolation trend). From the density plot, we see that the roughness distribution for the rupture segments has of mode of ~125 m and that the majority of the data fall below 250 m, confirming the smooth character of the seafloor prior to subduction.

3.2.2.2. South Andes

Because of its significant length, the Andean trench has been split up in two parts to facilitate quantitative comparisons, North and South Andes segments separated by the Arica bend. Almost all the trench length of the Southern Andes has recorded $M_W \geq 7.5$ ruptures (>90%), which are quite variable in age and magnitude. The two largest events in this area are the 1960 Bio-Bio M_W 9.6 rupture and the 2010 Maule M_W 8.8 rupture, which both occurred in the southernmost part of the trench (nos. 89 and 170 in Figure 7, respectively). The seafloor in front of these two rupture areas, south of the Juan Fernandez ridge, is shown to be one of the smoothest parts of the southern Andes margin (Lallemand et al., 2018). The area north of the Juan Fernandez ridge hosts relatively smaller ruptures, characterized by magnitudes mainly encompassed between M_W 7.5 and 8.0. The seafloor in front of this area is rougher than the area southward. The density plot shows that the majority of the roughness amplitudes are mainly below 250 m, the mode for the roughness in front of rupture segments being around 125 m.

3.2.2.3. Alaska-Aleutian

Like the preceding subduction zones, the Alaska-Aleutian region has a very high rupture length ratio; ~ 89% of the trench has ruptured. Almost half of the total number of $M_W \geq 7.5$ events in this area have magnitudes that are higher than M_W 8.5. Figure 7 shows that the seafloor in front of the Alaska-Aleutian trench on average is very smooth. Rough features are limited to the westernmost part, like the Detroit Tablemount and the Aleutian Rise. We observe that the main R_{LW} amplitudes for rupture segments are very low (mode of ~100 m, Figure 8c). The second mode associated with rupture segments, around 500 m, most likely results from the rough area in the west, facing the 1965 Rat Islands earthquake (M_W 8.7, no. 95 in Figure 7). This rupture seems to fade out toward the west. On the other side of the trench, we note that a rough domain is likely to be extended across the trench following a strong obliquity up to the area where event no. 95 stopped.

3.2.2.4. Andaman-Sumatra

The Sumatra-Java trench has also been divided into two segments: the Andaman-Sumatra segment in the north, starting from rupture no. 167 (Figure 7), and the Java-Sumba segment in the south. The

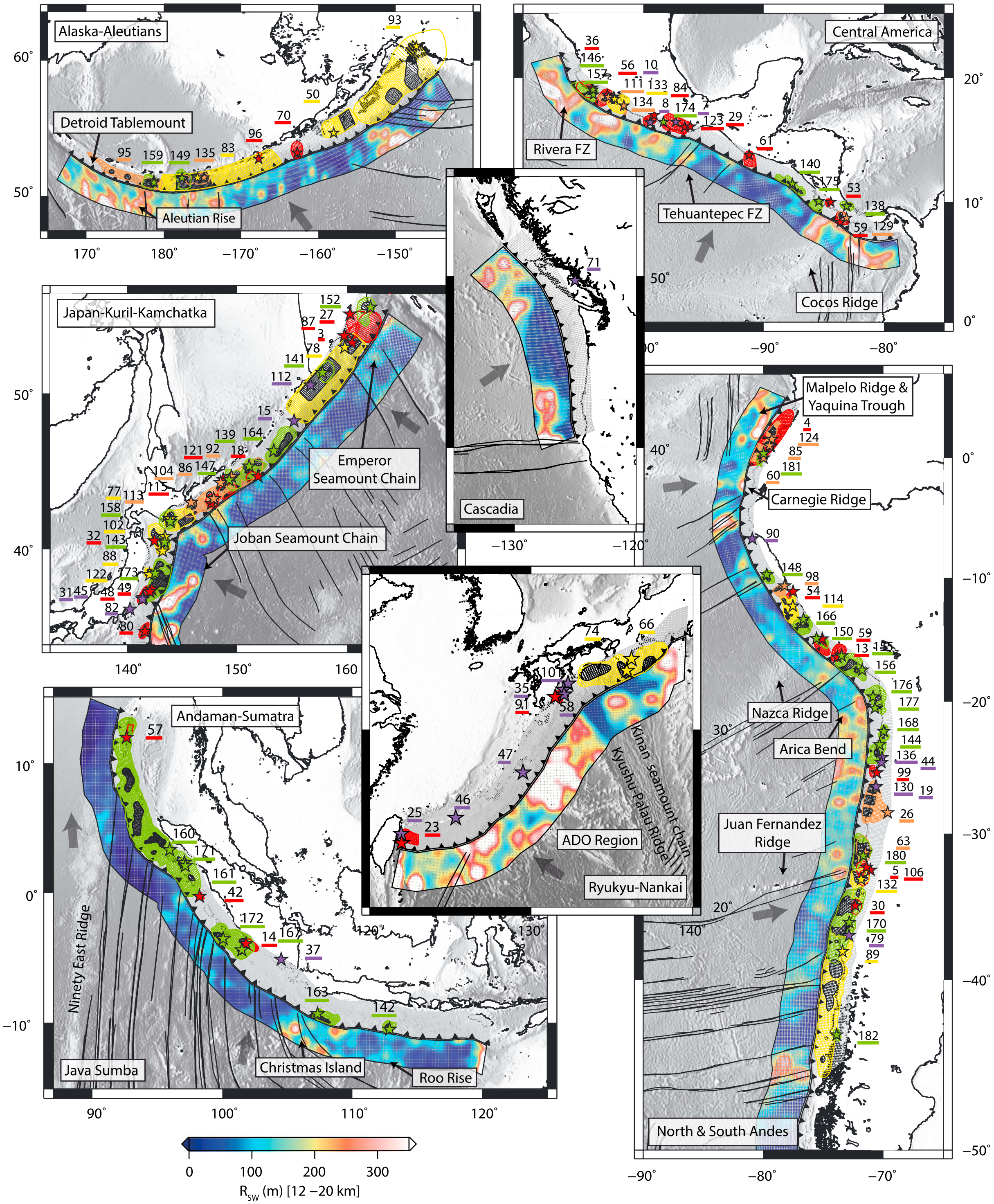

Figure 6. Short-wavelength roughness (R_{SW}) data and SubQuake grids for the six regions that have the highest occurrence of $M_W \geq 7.5$ interplate events and for Ryukyu-Nankai, Java-Suma, and Cascadia. Ruptures and epicenters are color-coded according to the rupture categories displayed in Figure 2; numbers indicate the events listed in Table 1. Seaward of the trench, short-wavelength roughness R_{SW} data from Lallemand et al. (2018) are plotted. Colors indicate the roughness amplitude. Seafloor features mentioned in the text are indicated. The ADO region (Ryukyu-Nankai) includes the Amami Plateau, Oki-Daito Ridge, and the Daito Ridge. Convergence directions are indicated by the dark-grey arrows.

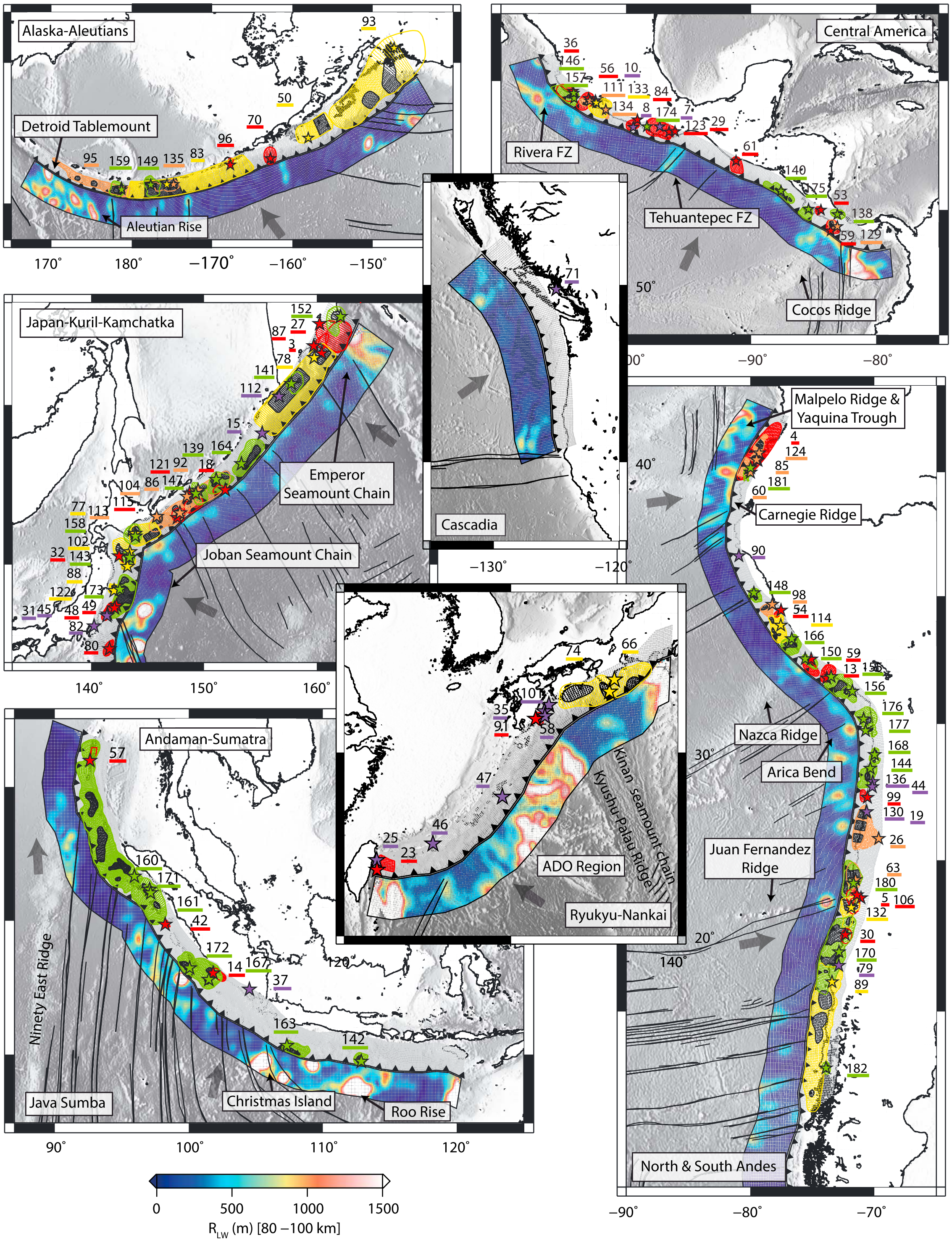

Figure 7. Long-wavelength roughness (R_{LW}) data and SubQuake grids for the five regions that have the highest occurrence of $M_W \geq 7.5$ interplate events and for Ryukyu-Nankai, Java-Suma, and Cascadia. Ruptures and epicenters are color-coded according to the rupture categories displayed in Figure 2; numbers indicate the events listed in Table 1. Seaward of the trench, long-wavelength roughness R_{LW} data from Lallemand et al. (2018) are plotted. Colors indicate the roughness amplitude. Seafloor features mentioned in the text are indicated. The ADO region (Ryukyu-Nankai) includes the Amami Plateau, Oki-Daito Ridge, and the Daito Ridge. Convergence directions are indicated by the dark-grey arrows.

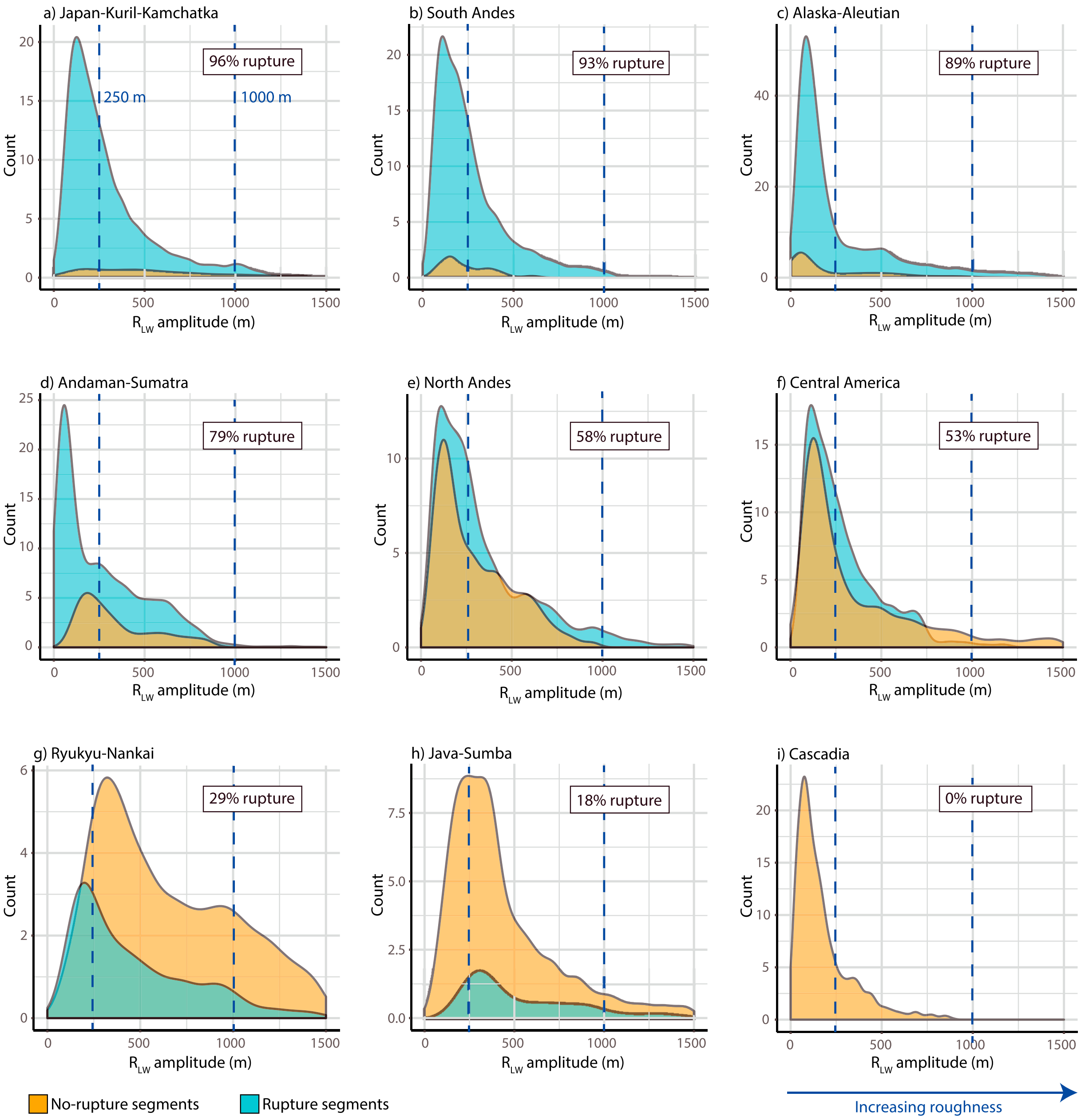

Figure 8. R_{LW} density plots for the nine regions mentioned in the text. Counts for long-wavelength roughness are shown with increasing roughness amplitudes (i.e., from smooth to rough). Orange and blue curves indicate the roughness data selected for the no-rupture and rupture segments, respectively. Blue dashed lines indicate the smooth and rough thresholds of 250 and 1,000 m, respectively (as introduced by Lallemand et al., 2018).

seafloor facing the Andaman-Sumatra trench contains very smooth patches, which alternate with rougher regions. These high roughness amplitudes are mainly caused by Ninety-East Ridge in the northwestern part of the area, almost parallel to the trench in the northernmost part and therefore not representative of the roughness of the subduction interface. The Andaman-Sumatra trench has recorded several large earthquakes: the $M_W \geq 8.5$ 2004, 2005, and 2007 ruptures, respectively, nos. 160, 161, and 167 in Figure 7. The density plot of this region (Figure 8d) shows the wide roughness signal observed in this area. Most of the rupture areas face very smooth seafloor, as suggested by the strong peak around a roughness amplitude of ~75 m. The higher roughness amplitudes characterizing rupture segments can be related to the Ninety-East Ridge and the rougher seafloor facing the 2007 rupture (no. 167).

3.2.2.5. North Andes

The part of the North Andes trench length that has ruptured (RLR ~ 58%) is considerably lower than in the Southern Andes (RLR ~93%). Right above the Arica bend, $M_W \geq 7.5$ ruptures are numerous, while in Northern Peru, a seismic gap is observed (Nocquet et al., 2014). The seafloor from the Arica bend up to this seismic gap region in Northern Peru is essentially smooth, while the seafloor in front of Ecuador and Colombia appears moderately rough (mainly because of the Malpelo Ridge, Carnegie Ridge, and the Yaquina Trough). Several ruptures occurred in this part of the Andean trench, such as the M_W 8.4 1906 event in Ecuador (no. 4 in Figure 7). When looking at the density plot (Figure 8e), the distribution of the R_{LW} roughness appears to be relatively similar for the rupture and no-rupture segments. This could be related to the rough area in the northernmost part, which might not be representative of the subduction interface roughness, since the Malpelo Ridge and Yaquina Trough are oriented subparallel to the trench and therefore may not extend into the trench. Furthermore, the seismic gap in northern Peru, facing smooth seafloor seaward of the trench, enhances the similarity between the rupture and the no-rupture curves.

3.2.2.6. Central America

The Central American subduction zone shows a moderate RLR, with ~53% of trench length that has ruptured. The seafloor in front of the trench is very smooth in the central part, while on the edges several rough areas occur (e.g., the Cocos Ridge in the southeast and the Rivera fracture zone in the northwest). The Tehuantepec fracture zone is also clearly visible in the center of the subduction zone. Many megathrust earthquakes occurred in the northern part of the Central America trench, offshore Mexico, where the roughness amplitudes significantly vary (Rivera fracture zone). Several M_W ~7.5 ruptures occur in the region where the Cocos Ridge is entering the trench, all of them being more or less limited to the ridge domain. The smooth segment in the middle, between the Cocos ridge and the Tehuantepec fracture zone, hosts very few megathrust ruptures. The density plot (Figure 8f) shows a somewhat higher count at low roughness for the rupture segments, but both curves follow a similar shape. For very high roughness amplitudes ($R_{LW} > 750$ m), the rupture segment count is close to zero, while the no-rupture distribution does include roughness amplitudes higher than 750 m. This is probably related to the signal east of the Cocos ridge, where we indeed have no record of any $M \geq 7.5$ earthquakes in the SubQuake database.

3.2.2.7. Ryukyu-Nankai

Even though the Ryukyu-Nankai trench only hosts four $M_W \geq 7.5$ ruptures (not taking into account the category 5 events), they still take up 29% of the trench length (“moderate RLR” class). In terms of seafloor roughness, the area as a whole is considered rough, because several ridges with high R_{LW} amplitudes (i.e., the Kyushu-Palau Ridge, Amami Plateau, Oki-Daito Ridge, and the Daito Ridge) are intersecting the trench. However, the area in front of the two largest ruptures in this region (i.e., the 1944 Tonankai and 1946 Nankaido earthquakes, nos. 66 and 74 in Figure 7) appears to be smoother. The assumption that the roughness signature seaward of the trench can be extrapolated perpendicularly into the trench is supported by the subducting Kinan Seamount Chain and the Kyushu-Palau ridge, since both have been imaged on the subducting interface (Kodaira et al., 2000; Lallemand, 2016; Yokota et al., 2016). It is also known that many historical earthquakes have occurred in the 1944 Tonankai and 1946 Nankaido rupture areas (e.g., Ando, 1975; Satake, 2015) while the number of earthquakes in the remaining part of the Ryukyu trench is very low. These observations are in agreement with the density plot (Figure 8g); the no-rupture segments are mainly characterized by very rough R_{LW} amplitudes, and a relatively large part of the data exceeds the 1,000-m threshold.

3.2.2.8. Java-Sumba

The Java-Sumba trench has a low rupture length ratio, with only 18% of the trench length that has ruptured. The two ruptures that did occur in this area had magnitudes between M_W 7.5 and 8.0 (nos. 142 and 163 in Figure 7). As can be seen in Figure 7, the Java-Sumba section is very rough, mainly because of the Roo Rise and the Christmas Island topographic highs in the central part. The density plot (Figure 8h) shows roughness distributions similar for the rupture and no-rupture segments, with a mode of ~300 m for both distributions. The range of roughness amplitude for the two rupture segments in this region does not significantly differ from the one of the remaining areas of the trench.

3.2.2.9. Cascadia

The SubQuake database records only one event in the Cascadia subduction zone: a M_W 7.5 earthquake in 1946 (category 5). However, this event was most likely a crustal or intraplate event (Clague, 2002). The prior-to-subduct seafloor does appear very smooth, which can be seen both from Figure 7, as from the

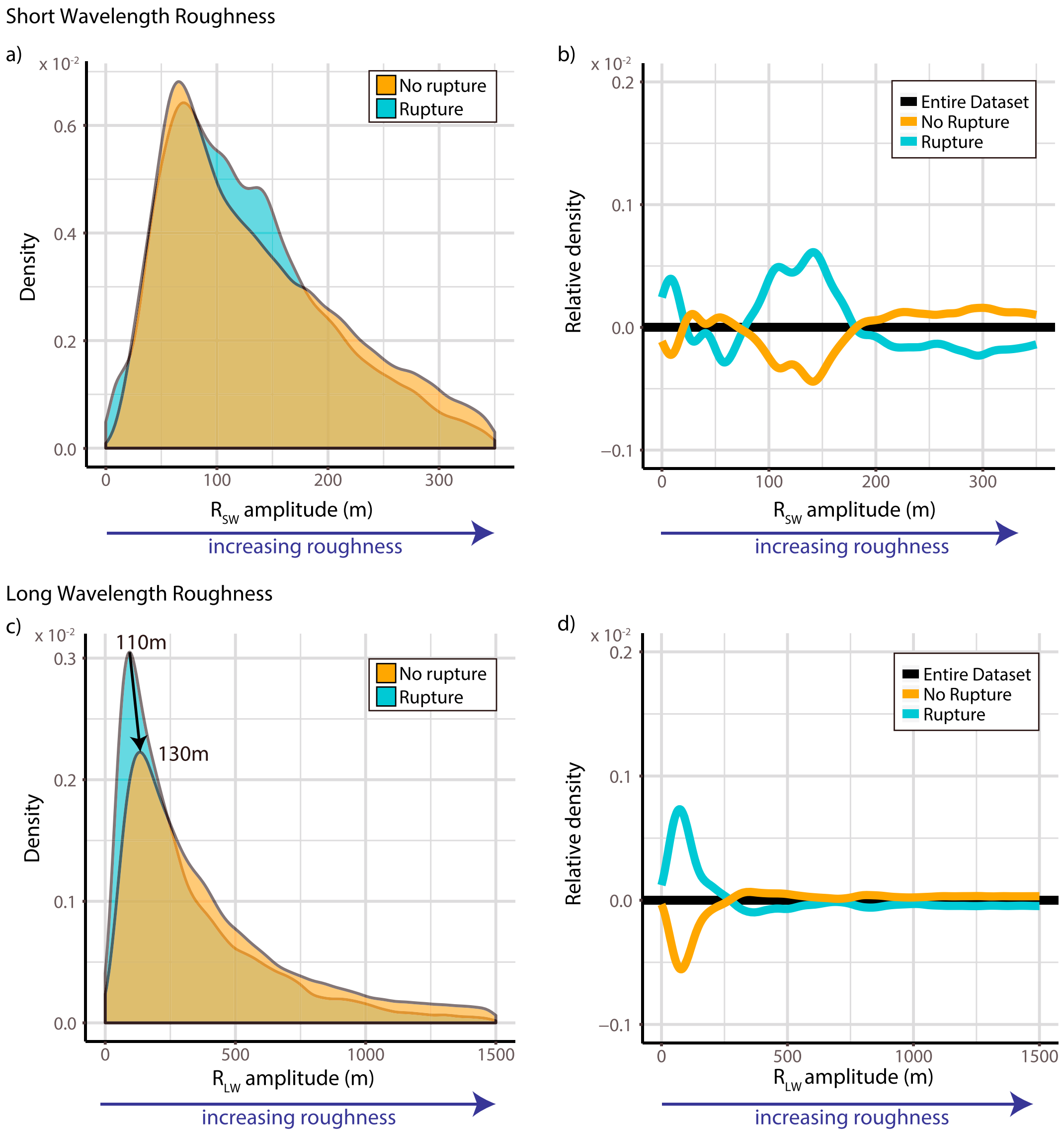

Figure 9. Global density distributions, taking into account all subduction zones and shown for both short-wavelength roughness (a, b) and long-wavelength roughness (c, d). Orange and blue shades indicate the roughness data selected for the no-rupture and rupture segments, respectively. Plots (a) and (c) show the density curve for increasing roughness amplitudes, from smooth (left) to rough (right). Plots (b) and (d) show the relative density, which illustrates the deviation of the two segment classes with respect to the entire data set.

density plot (Figure 8i), which shows that the large majority of roughness data fall below 250 m. This distribution is very similar to regions with a large rupture length ratio, such as Japan-Kuril-Kamchatka and Alaska-Aleutian. Even though no interplate $M_W \geq 7.5$ events have been recorded during the past 117 years, it is widely accepted that great earthquakes have occurred before this time period (Wang & Tréhu, 2016). This is supported by coastal geological studies (Atwater, 1987), marine turbidity deposits (Adams, 1990; Goldfinger et al., 2012), and also by historical Japanese tsunami records (Satake, 2003).

3.2.3. Rupture Areas: Global Comparison

In this section, we study all subduction zones together. Figure 9 shows the density plots for the whole data set, both for the short- and long-wavelength roughness. It also displays the relative density function, which measures the offset of the two subgroups with respect to the whole data set (a combination of both the rupture and no-rupture subsets):

$$D_{\mathrm{rel}}(R) = D_{\mathrm{sub}}(R) - D_{\mathrm{all}}\ (R)$$

where D_{rel} is the relative density at a specific value for roughness R, D_{sub} is the density for each subset (i.e., rupture versus no-rupture), and D_{all} is the density for the entire data set.

Such a relative density plot helps visualizing the difference between the two classes of trench segments especially since often the curves are rather similar in shape. This is related to the global distribution of the roughness data, which shows that the highest densities are usually at roughness amplitudes between 50 and 150 m for R_{SW} and 0 and 500 m for R_{LW}, regardless of the rupture or no-rupture class they make part of. With the relative density plots, we highlight the offset of both the rupture and no-rupture subsets with respect to the density signal of the entire data set. Negative relative densities indicate that densities are lower than the overall density signal, while positive relative densities show a density increase with respect to the overall signal. Depending on the roughness amplitudes at which these variations occur, we can infer whether smooth or rough seafloor is mainly associated with rupture or no-rupture segments. For the short-wavelength roughness, we do not observe a significant difference between the rupture and no-rupture segments (Figures 9a and 9b). Regarding the long-wavelength roughness, rupture segments have higher densities at low roughness amplitudes (i.e., smooth seafloor) than the no-rupture segments (Figures 9c and 9d). Conversely, the no-rupture segments have slightly higher densities at higher roughness amplitudes. This switch in density dominance takes place at a roughness amplitude of ~250 m. In addition, the mode of the no-rupture class is shifted to the right with respect to the rupture class, showing a difference in R_{LW} of ~20 m. These results indicate that when looking at long-wavelength roughness, ruptures tend to occur preferentially on smooth portions of the subduction megathrust.

3.2.4. Rupture Areas: Comparison for Different M_{W} Groups

Another aspect of the quantitative comparison we performed is the relationship between subduction interface roughness and varying moment magnitude. Instead of considering rupture segments (often consisting of several, partly overlapping ruptures), we now select the seafloor roughness facing each event and calculate a mean roughness value. Figure 10a shows mean R_{LW} versus M_{W} of cat. 1–4 events. We observe that for decreasing roughness, the moment magnitude increases, following a power law relationship. This result is especially clear for the $M_{\mathrm{W}} > 8.5$ events, which all show an average roughness lower than ~300 m. An exception is the 1965 Rat Island event (category 3), for which it has already been mentioned that the roughness proxy might not be entirely representative. The M_{W} 8.0–8.5 events show a wider range of average roughness values but are all smaller than 700 m, except for the 1923 Kamchatka and 1920 Taiwan events, which are both category 4 events and therefore less reliable. For the M_{W} 7.5–8.0 events, we see a wide range of roughness amplitudes, ranging up to 1,750 m. Figures 10b–10e show density and relative density plots when only considering ruptures with M_{W} 7.5–8.5 (b and c) or $M_{\mathrm{W}} > 8.5$ (d and e). For this comparison, previous rupture segments (that would switch into no-rupture segments due to the modified magnitude threshold) are excluded from the computation. For the $M_{\mathrm{W}} \geq 8.5$ ruptures, we observe a very clear difference between the roughness signals for the rupture segments with respect to the no-rupture segments. These results indicate that mainly the $M_{\mathrm{W}} \geq 8.5$ ruptures are promoted by a smooth subducting interface at long wavelengths.

3.2.5. Seismic Asperities

We now focus on the regions where the maximum slip occurred: the seismic asperities. Their roughness signal is compared to the distribution for rupture segments in general, to see if there is a difference between the maximum slip areas and remaining rupture areas. Figure 11 shows relative density plots for both R_{LW} and R_{SW}, highlighting the difference in roughness distribution with respect to rupture areas in general and the roughness distribution of the entire global data set (black line). The reason why the signal for seismic asperity segments is compared to the signal of all rupture areas (including the seismic asperities) comes from the fact that ruptures and seismic asperities often overlap. A seismic asperity for one event might be part of the rupture area for a second event, without being highlighted as a seismic asperity for that second event. For R_{LW}, we observe that the roughness distribution for seismic asperity segments shows the same pattern as for the rupture segments with respect to the entire data set (i.e., higher densities at low roughness amplitudes and lower densities at high roughness amplitudes). However, the seismic asperity signal is more amplified, indicating that the seafloor in front seismic asperities is smoother than in front of the rupture areas in general. This amplification of the signal is also seen for the short-wavelength roughness, even though no clear difference in R_{SW} signal between rupture and no-rupture areas was observed.

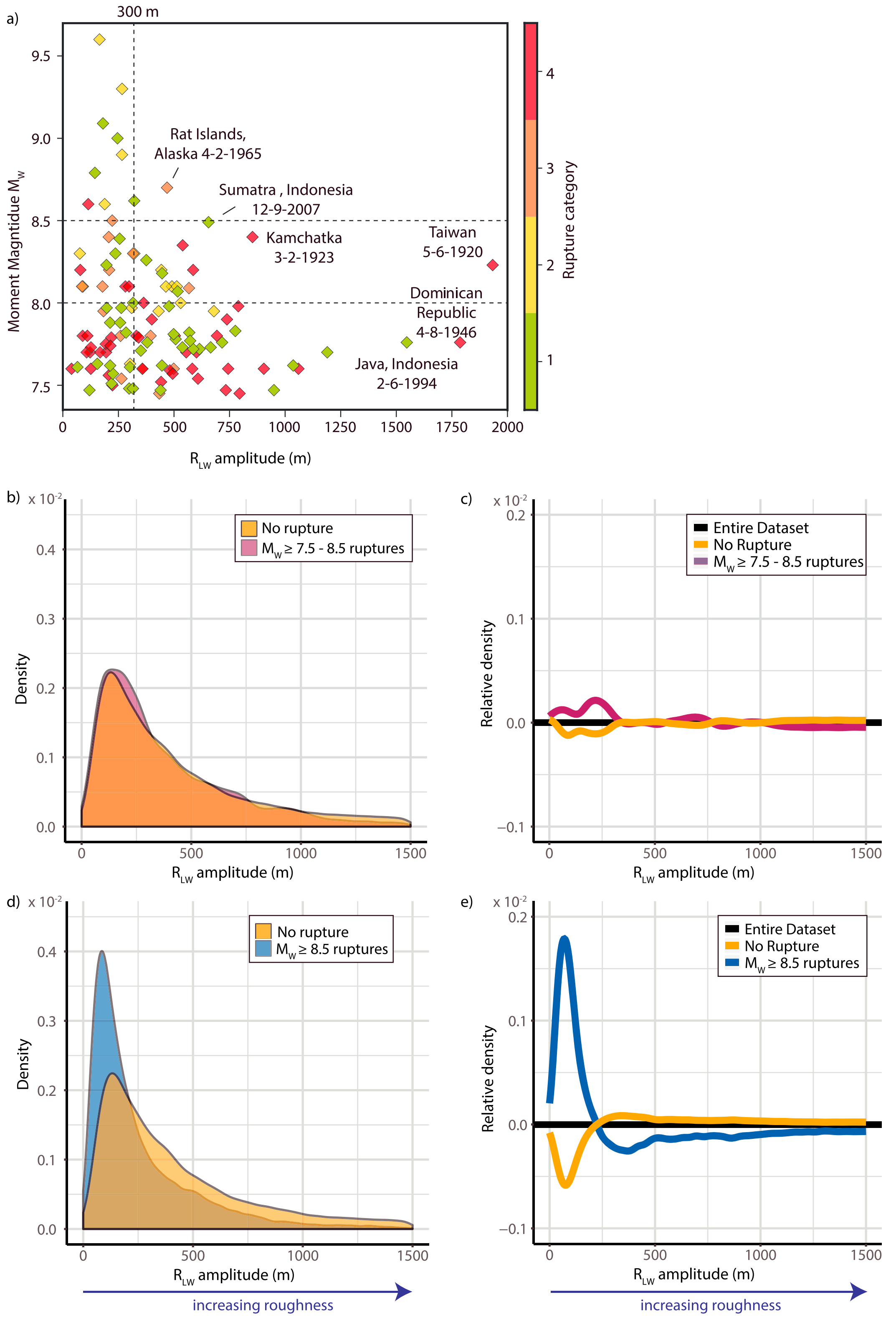

Figure 10. Long-wavelength roughness distribution (R_{LW}) with varying moment magnitudes. (a) Average R_{LW} for each event versus moment magnitude. Possible outliers are indicated with their name and date. Events are color-coded according to the rupture categories. Global density distribution for R_{LW}, only taking into account M_W 7.5–8.5 ruptures (b), or $M_W > 8.5$ only (d), and relative density distribution (c and e, respectively) are displayed as well.

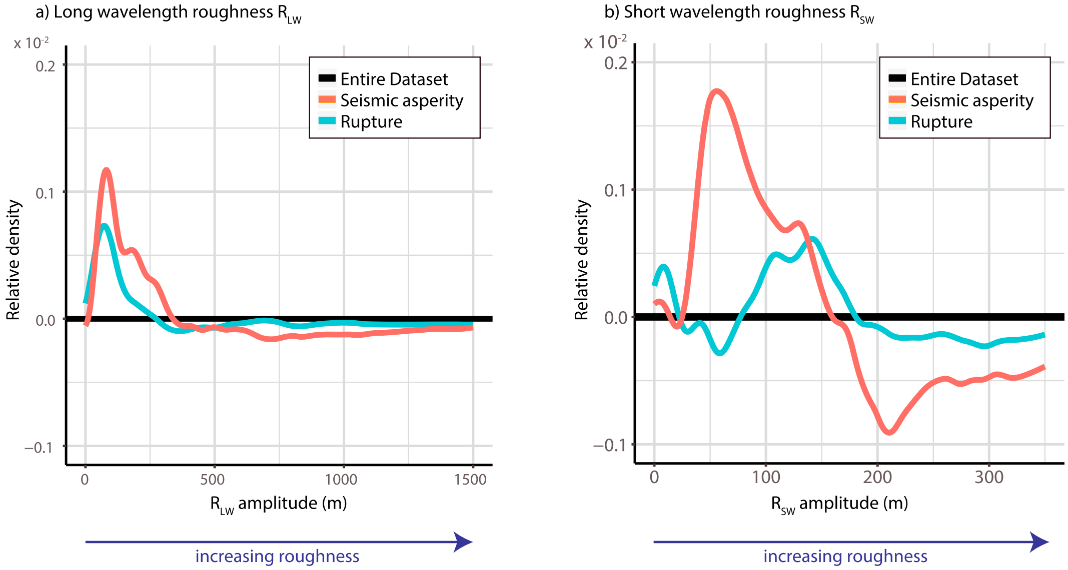

Figure 11. Relative density distribution for R_{LW} (a) and R_{SW} (b) for seismic asperities (pink curves) and rupture segments (blue curves) with respect to the global roughness distribution (black line).

3.2.6. Epicenters

Figure 12 shows relative density plots for 182 $M_{\mathrm{W}} \geq 7.5$ epicenters as a function of the seafloor roughness. Both for short- and long-wavelength roughness, epicenters correlate with slightly rougher seafloor than average, around 125 m for R_{SW} and 600 m for R_{LW}. To test the robustness of this result, the same algorithm has been performed for 100 synthetic data sets (grey lines in Figure 12), each containing 182 randomly selected grid nodes instead of the real epicenters used for the original comparison. The grey lines in Figure 12 form an envelope that demonstrates the disparity in roughness signal that can arise from simply

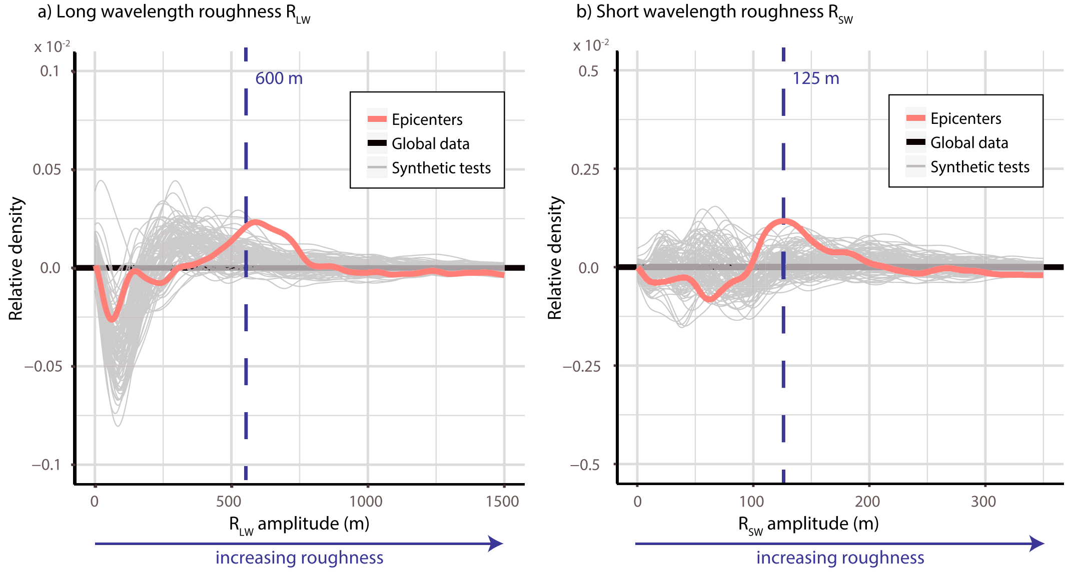

Figure 12. Relative density plots for roughness data selected for epicenters (pink curves) with respect to the global roughness distribution (black line), both for R_{LW} (a) and R_{SW} (b). The grey curves indicate the relative density for 100 synthetic data sets, each containing roughness data for 182 randomly selected grid nodes, which represent the "synthetic epicenters."

selecting a subset of the total data set. The roughness distribution associated with the real epicenters of the SubQuake database falls partly outside this envelope.

4. Discussion

The possible relationship between the roughness of the subduction interface and the occurrence of megathrust earthquakes remains a subject of debate. So far, this relationship has not been tested by using a quantification of the seafloor roughness (Lallemand et al., 2018) and taking into account all large interplate events since 1900.

We provide a global database (SubQuake), which includes the location of the rupture epicenter, the overall rupture area, and the region where the largest displacement occurs (the seismic asperity). This database is designed to perform a quantitative comparison with two roughness parameters provided by Lallemand et al. (2018): the short-wavelength roughness R_{SW} (12–20 km) and the long-wavelength roughness R_{LW} (80–100 km). As for many studies attempting to unravel some relevant characteristics for subduction megathrust earthquakes, the limited time record of such events may alter the results (Stein & Okal, 2007, 2011). In this study we therefore tried to limit this problem by using the largest possible time window for our analysis, 1900–2017. We are aware that this approach raises other uncertainties, such as the decreasing quality of rupture and/or seismic asperity contours for older ruptures. However, we show that despite these uncertainties, a first-order global trend can be observed.

Ruptures with $M_W \geq 7.5$ tend to occur more often on smooth subducting seafloor at long wavelengths, which is especially significant for the $M_W > 8.5$ events. When focusing on the seismic asperity segments, we observe that they tend to correlate better with smooth seafloor than rupture areas in general. For the epicenter correlation, we see a slight difference in roughness signals, which suggests a possible physical relationship between the nucleation of a rupture and the roughness of the subduction interface. Below, we will discuss these main findings in more detail, with respect to previous studies.

4.1. $M_W \geq 7.5$ Ruptures Tend to Occur More Often on Smooth Subducting Seafloor

The fact that $M_W \geq 7.5$ megathrust events preferably occur in regions adjacent to a smooth subducting seafloor is in agreement with previous studies (Bassett & Watts, 2015; Das & Watts, 2009; Wang & Bilek, 2014), which compared the variations in bathymetry with the occurrence of megathrust events in a qualitative way. We show that this pattern is not only true for specific ruptures or subduction zones but that it is a general pattern, mainly observed for long-wavelength seafloor roughness (Figures 9c and 9d). By simply looking at the overall roughness and the occurrence of megathrust events, we see that most trenches where seismic slip is spatially predominant are also among the smoother regions (i.e., Japan-Kuril-Kamchatka, South Andes, and Alaska-Aleutians). Those regions, in combination with the very rough areas where almost no $M_W \geq 7.5$ events have been observed (e.g., Izu-Bonin-Mariana), play an important role in the negative correlation between seafloor roughness and $M_W \geq 7.5$ events that we observe in this study. However, within this global trend, exceptions exist, which we briefly discuss in the following paragraphs. One region that does not face smooth seafloor everywhere, but still hosted many seismic ruptures, among which three $M_W > 8.5$ events, is the Andaman-Sumatra trench. Many of the high roughness amplitudes observed along this trench result from the presence of the Ninety-East ridge. Whether this Ninety-East Ridge is continuing into the subduction interface, however, is questionable (Moeremans & Singh, 2014, 2015). Toward the Andaman Islands, the ridge becomes almost parallel to the trench. In this region, it is therefore possible that the seafloor in front of the trench does not provide a good proxy of the actual subduction interface roughness. Moreover, the large amount of trench sediments (Heuret et al., 2012) in this area suggests that the subduction interface could be considerably smoother than the proxy used in this study. Several regions that do not fit the general pattern either, are the Cascadia and Antilles subduction zones, as well trench segments in Northern Peru and Central America. These areas all face smooth seafloor, especially at long wavelengths, but show very low to no occurrence of large megathrust events. The Cascadia subduction zone has been studied extensively (Adams, 1990; Atwater, 1987; Goldfinger et al., 2012; Satake, 2003), and it is widely accepted that previous great megathrust events have occurred along this subduction zone, the last one most likely around 1700. The recurrence time of these events is thought to be ~500 years (Wang & Tréhu, 2016), which explains why no interplate events have been recorded during the past 117 years.

Regarding the smooth region in Northern Peru, Nocquet et al. (2014) used geodetic analyses to demonstrate that this area behaves mainly aseismically, indicating that even though the interface seems to be smooth, other factors play a role in the lack of seismicity. The lack in recently recorded megathrust events remains more difficult to explain for the Antilles subduction zone, as well as the central part of the Central America trench (in front of Guatemala, El Salvador, and Nicaragua). In these cases, only little information on the geodetic coupling exists, which makes it difficult to infer whether the subduction interface is predominantly creeping or locking (Okal & Hartnady, 2009). Both the Puerto Rico and the Lesser Antilles trench are thought to be only partially coupled (Manaker et al., 2008), while the Central America trench between South Mexico and El Salvador is deemed to be weakly coupled (coupling degree of ~0.25, Franco et al., 2012). This low-coupled Central America segment is thought to have been influenced by the subduction of the Cocos Ridge toward the southeast, which may act as an indenter against the Caribbean plate (LaFemina et al., 2009; Scholz & Campos, 2012). Other possible influences on the coupling and seismogenic behavior are fluid overpressures (Saffer & Tobin, 2011) and the inheritance of previous subducted features, which could have damaged the overriding plate and therefore, despite the smooth incoming seafloor, prohibit the occurrence of large events (Ranero & von Huene, 2000).

4.2. $M_W > 8.5$ Events Are More Sensitive to a Smooth Seafloor Than Lower Magnitude Ruptures

A clear result from our global analysis is the improved correlation between subduction interface roughness and megathrust ruptures with high earthquake magnitude (Figure 10a). When we study the relationship between only M_W 7.5–8.5 events and facing seafloor roughness, we observe almost no difference between the roughness signals for seismic event segments and for the remaining regions (Figures 10d and 10e). However, if we focus on earthquakes with higher magnitudes (i.e., $M_W > 8.5$), we see that it is mainly these largest events that contribute to the negative correlation between megathrust earthquakes and seafloor roughness (Figures 10b and 10c). In other words, our analysis shows that the largest events are the ones that might have been mostly favored by a smooth subducting seafloor. Since the moment magnitude of an event is proportional to the rupture area, the larger the event can grow, the higher the magnitude. A smooth seafloor without any large mechanical/frictional obstacles or barriers is therefore the ideal location for an event with the potential of becoming a great megathrust earthquake. For smaller events, however, two main reasons could explain why they are not be able to grow larger and reach higher magnitudes: (1) Their initial energy is too low. The relationship between the initial stages of a rupture (i.e., the rupture nucleation phase) and the final magnitude is debated. It has been proposed that larger nucleation zones should result in earthquakes with larger magnitudes (e.g., Ohnaka, 2000), whereas others argue that the nucleation size is unrelated to the final size of an earthquake (e.g., Lapusta & Rice, 2003). 2) A heterogeneous stress distribution on a fault, either due to the arrest of previous ruptures (i.e., areas where stress has been released recently) or due to the presence of a physical barrier (e.g., a subducting seamount or ridge), could prohibit events from propagating and therefore growing any further (Corbi et al., 2017; Lay et al., 1982). In this case, relatively small ruptures will occur more often on seafloor that is slightly rougher and therefore more heterogeneous, while smooth seafloor might facilitate great to giant earthquakes. This trend has also been observed on the laboratory scale and with numerical simulations. Goebel et al. (2017) investigated the influence of fault roughness on *b*-values, focal mechanisms, and spatial localization of laboratory acoustic emission events during stick-slip experiments. They observe that smooth faults promote a more homogeneous stress field and therefore larger rupture sizes when compared to rough or fractured fault interfaces. Zielke et al. (2017) performed large-scale numerical simulations, while varying roughness and strength conditions. They show that smoother faults may generate larger earthquakes than rougher faults under identical tectonic loading conditions.

On the scale of the subduction megathrust, a clear example of the variable roughness dependency with moment magnitude can be seen along the South Andes trench. Here the two greatest ruptures (i.e., the 1960 M_W 9.6 and the 2010 M_W 8.8, events 89 and 170 in Figure 7) occurred in the southernmost part of the trench, where the seafloor is continuously very smooth. Toward the north, the seafloor is characterized by smooth patches alternating with rough features, and here mainly M_W 7.5–8.0 ruptures occurred. The fact that $M_W > 8.5$ events are more frequently associated with a smooth seafloor might therefore be a direct consequence of the fact that most of these very large ruptures needed continuous smooth seafloor to propagate over long trench-parallel distances and to reach these maximum magnitudes (Figure 13). An exception is the

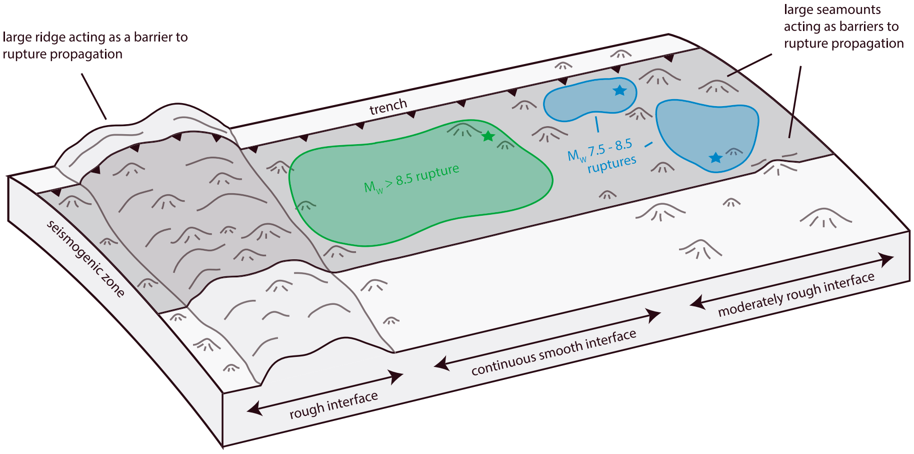

Figure 13. Conceptual model illustrating the main results of this study. $M_W > 8.5$ ruptures tend to occur more often on a smooth subduction interface segment, while M_W 7.5–8.5 ruptures might also occur on moderately rough seafloor, characterized by a mix of smooth and rough patches. Subducting features, like seamounts or ridges, might act as barriers to rupture propagation but could also be the regions where ruptures nucleate, due to the transition between a locked and creeping state of the interface.

2011 Tohoku event, which reached a M_W of 9.1 without propagating over large trench parallel distances, due to extremely high slips observed in the rupture area (Yue & Lay, 2013). Following the reasoning above, we would expect to see a steady correlation increase with increasing magnitudes, that is, to observe a larger difference between roughness signals facing M_W 7.5–8.0 ruptures than facing the $M_W > 8.0$ ruptures. This can be seen in Figure 10a. However, this trend could be influenced by the larger uncertainty in the seafloor roughness proxy when considering lower magnitude events and therefore smaller rupture areas. We mainly focus on the trench-parallel correlation with the seafloor roughness, while earthquakes with $M_W < 8.0$ might not grow necessarily in the trench parallel direction (Sparkes et al., 2010). Besides this, the number of category 5 ruptures (62 events), for which we were not able to obtain a rupture contour, could influence this result. These events are mainly among the oldest events in the database, which makes their location, magnitude, and also their belonging to the subduction interface very uncertain.

4.3. Short-Wavelength Versus Long-Wavelength Roughness

An important aspect of the correlations performed in this study is the considered wavelength of the seafloor roughness. Do all roughness wavelengths play a role in facilitating or prohibiting the occurrence of large interplate earthquakes? We do not observe a significant correlation between the short-wavelength roughness (12–20 km) of the seafloor in front of the trench, when looking at segments that correlate with $M_W \geq 7.5$ megathrust ruptures versus the remaining length of the trench (i.e., where no ruptures have been recorded since 1900; Figures 9a and 9b). For the long-wavelength roughness (80–100 km), we do observe a difference in roughness amplitudes when comparing rupture and no-rupture segments. Several possible explanations why we do not see a similar result when looking at smaller spatial scales may be suggested: (1) It is possible that variations in seafloor roughness at shorter wavelength and therefore lower amplitudes (i.e., in the range of 0–350 m) are not significant enough to play a role in rupture propagation and arrest. In the Alaska-Aleutian region, for example, we observe a very different roughness signal when we look at the two wavelength bandwidths (Figures 6 and 7). At long wavelengths, the roughness amplitudes are very low, and the region has been therefore classified as smooth by Lallemand et al. (2018). The short-wavelength roughness map, however, shows much more variability in roughness, ranging up to amplitudes larger than 350 m. Despite the relatively rough seafloor at short wavelength, many $M_W > 8.0$ ruptures have occurred in this area, making it one of the regions that have a high rupture length ratio. (2) The proxy for the subduction interface roughness at short wavelength based on the seafloor bathymetric prior to subduction could be less reliable. In this study, we assume that the seafloor seaward of the trench is a reasonable proxy for the roughness of the subduction interface. For the long wavelengths, this proxy is likely to be valid (e.g., Bassett & Watts, 2015; Das & Watts, 2009; Kodaira et al., 2000; Mochizuki et al., 2008), but one can imagine that the shorter the wavelengths, the more difficult it is to extrapolate roughness variations over a distance of several hundreds of kilometers into the subduction interface.

4.4. Seismic Asperities Correlate With Smoother Seafloor Than Ruptures in General

From our analysis of seafloor roughness facing seismic asperities, we observed an amplification of the signal, with respect to the pattern observed for rupture segments (Figures 11a and 11b). This indicates that the seafloor in front of seismic asperities alone is smoother than the seafloor in front of rupture areas in general. This is in line with expectations, since it seems plausible that during rupture propagation the largest amount of slip occurs where the seafloor is the smoothest, since this is where the largest coupling is expected (Contreras-Reyes et al., 2010, 2017). Surprisingly, we also observe an excess in low R_{SW} amplitudes (~50–60 m), which is not observed for the areas facing the ruptures in general. This may indicate that seismic asperities preferentially locate where the plate interface is smooth at all wavelengths. A more detailed relationship between seismic asperities and subduction interface roughness cannot be obtained by this study, since some seismic asperities might be too small for the purpose of our global analysis, and their exact location, even for recent events, remains quite uncertain (Clévédé et al., 2012; Lay, 2017). Therefore, future studies, possibly more focused on the propagation of individual ruptures, are needed to confirm this (e.g., Ye et al., 2018).

4.5. Possible Link Between Rupture's Nucleation and Seafloor Roughness

As mentioned before, when studying the spatial occurrence of large megathrust earthquakes, it is important to take into account the rupture area of these events and not just the location of their hypocenters. However, by studying solely the hypocenter location, we might gain some insights about the conditions favoring rupture nucleation. According to the rupture data compiled in this study, we see that for ~35% to ~50% of ruptures, the epicenter is located outside the seismic asperity (37% taking into account all seismic asperities, 47% for category 1 events only). This indicates that the nucleation point of an earthquake does not necessarily occur where the largest displacement takes place. Therefore, the conditions necessary for earthquake nucleation are likely to be different than the ones that favor earthquake propagation. Large events have been suggested to nucleate in the vicinity of transition between locked and creeping patches of the subduction interface (Lapusta & Rice, 2003). Such transitional regions could result from a change in interface roughness, like the base of a seamount or ridge (Das & Watts, 2009). We observe that the location of a rupture epicenter correlates with a slightly rougher seafloor (compared to the average seafloor, section 3.2.6, Figures 12a and 12b). This result has been tested for robustness with 100 synthetic tests (see section 3.2.6. and supporting information). The actual epicenter data fall partly outside the envelope formed by the synthetic tests for the long-wavelength roughness, suggesting that the results we obtain are robust and might indicate a physical relationship between the nucleation of a rupture and the roughness of the subduction interface. In regions close to subducting topographic highs, the stress conditions at the resulting transition between locked and creeping fault patches might be favorable for rupture nucleation. Of course, for this we would assume that major subducting highs would favor a dominantly creeping behavior (Wang & Bilek, 2011).

4.6. Seafloor Roughness Acting as a Barrier to Rupture Propagation

Numerous authors have suggested that topographic features on the seafloor, like seamounts or ridges, may segment the subduction interface and arrest ruptures (Geersen et al., 2015; Kodaira et al., 2000; Mochizuki et al., 2008; Robinson et al., 2006; Wang & Bilek, 2011). Such behavior has been observed for the 2011 M_W 9 Tohoku rupture, which stopped against the Joban seamount chain toward the south (Wang & Bilek, 2014), but also for the 1960 M_W 9.6 Bio-Bio rupture, which is thought to be influenced by the subducting Chile Rise at the southernmost part of the rupture area (Contreras-Reyes & Carrizo, 2011). The southern arrest of the 2004 M_W 9 Sumatra earthquake is also thought to have been caused by a morphological high, which acted as a persistent barrier and therefore prevented the 2004 and 2005 Sumatra ruptures from occurring as one single event (Morgan et al., 2017). Despite the many examples of subducting highs that likely played a role in rupture arrest, it is not easy to address this question in this global study. Many rupture areas in our SubQuake grid overlap, making it difficult to define the areas that may have acted as barriers to rupture propagation. An additional complexity arises from the possible change in mechanical behavior of a subducting feature over time, for example, depending on the slip history of preceding events or the mechanism that causes the barrier-type behavior (i.e., either due to locally increased or decreased coupling at the subducting high; Das & Watts, 2009; Kodaira et al., 2000; Morgan et al., 2017; Wang & Bilek, 2011). Even though we cannot address the role of subducting reliefs as barriers in detail, our results do highlight a general trend of rupture occurring preferentially on large smooth patches of the seafloor, especially with increasing rupture magnitude. This is in line with earlier proposed models for seamount subduction, which stated that a seamount might fracture the overriding plate while it subducts and therefore would locally prevent the buildup of stress necessary for rupture propagation (Dominguez et al., 1998; Ruh et al., 2016; Wang & Bilek, 2011, 2014). In addition, Lallemand et al. (2018) have shown that rough seafloor is associated with low values of seismic coupling (<0.5), while smooth seafloor correlates with high seismic coupling (>0.5). Seafloor that is characterized as rough, with many significant topographic features, might therefore be less prone to host large to giant earthquakes. This is what we observed in this study as a first-order global relationship. Besides the studies that address natural examples of subducting features and their role on the seismogenic behavior of the megathrust, modeling studies, focusing on the physical mechanism of relief subduction, are necessary to unravel the effect that a topographic high might have on the state of stress and on the coupling along the subduction interface.

5. Conclusions

We present SubQuake: a complete catalogue of $M_W \geq 7.5$ subduction interplate earthquakes that occurred between 1900 and 2017. SubQuake includes information on the rupture epicenter, rupture contour, and seismic asperity contours. We use this database for a quantitative comparison with a proxy of the subduction interface roughness within a given wavelength interval (12–100 km). From this global comparison, we can draw the following conclusions:

1. Large ($M_W \geq 7.5$) interplate earthquakes occurred preferentially in areas that are characterized by smooth seafloor. From this group, $M_W > 8.5$ earthquakes are the most sensitive to a smooth subduction interface, while for M_W 7.5–8.5 events, the difference in roughness pattern with respect to the areas that did not host any events is less clear.
2. We observe that roughness at longer wavelengths (80–100 km) seems the most determining for the occurrence of large to giant subduction earthquakes. For short-wavelength roughness, we do not observe a clear difference in roughness signal between rupture and no-rupture areas.
3. Based on our analysis, seismic asperities tend to correlate better with smooth seafloor than rupture areas in general, both for short and long wavelengths.
4. Our first-order comparison between rupture epicenters and seafloor roughness suggests that there might be a physical relationship between the nucleation of a rupture and the roughness of the subduction interface.

Future studies are necessary to systematically investigate the role of seafloor roughness on the coupling along the subduction interface and on the occurrence of large to giant megathrust earthquakes. Modeling studies, both analogue and numerical, can contribute to the understanding of the role of subducting features over timescales of multiple seismic cycles. Additional natural data studies, for example, focusing on the geodetic coupling of specific areas, are necessary to better understand the current state of stress in regions where rough seafloor is subducting.

Acknowledgments
We thank Anthony Sladen and two anonymous reviewers for providing detailed and constructive comments to improve this study. We are grateful to Dan Bassett for sharing the rupture data he collected with us and to Paul Martin Mai and Gavin Hayes for providing the SRCMOD and USGS databases, both containing many rupture models we used to compile our database. The SubQuake data can be downloaded via subquake.gm.univ-montp2.fr. This project has received funding from the European Union's Horizon 2020 research and innovation program under the Marie Sklodowska-Curie grant agreement 642029—ITN CREEP.

References

Acharya, H. K. (1980). Seismic slip on the Philippine fault and its tectonic implications. *Geology*, *8*(1), 40–42. https://doi.org/10.1130/0091-7613(1980)8<40:SSOTPF>2.0.CO;2

Adamek, S., Tajima, F., & Wiens, D. A. (1987). Seismic rupture associated with subduction of the Cocos Ridge. *Tectonics*, *6*(6), 757–774. https://doi.org/10.1029/TC006i006p00757

Adams, J. (1990). Paleoseismicity of the Cascadia subduction zone: Evidence from turbidites off the Orgeon-Washington margin. *Tectonics*, *9*(4), 569–583.

Allen, T. I., & Hayes, G. P. (2017). Alternative rupture-scaling relationships for subduction interface and other offshore environments. *Bulletin of the Seismological Society of America*, *107*(3), 1240–1253. https://doi.org/10.1785/0120160255

Ammon, C. J., Ji, C., Thio, H.-K., Robinson, D., Ni, S., Hjorleifsdottir, V., et al. (2005). Rupture process of the 2004 Sumatra-Andaman earthquake. *Science (New York, N.Y.)*, *308*(5725), 1133–1139. https://doi.org/10.1126/science.1112260

Ando, M. (1975). Source mechanisms and tectonic significance of historical earthquakes along the Nankai trough, Japan. *Tectonophysics*, *27*(2), 119–140. https://doi.org/10.1016/0040-1951(75)90102-X

Atwater, B. F. (1987). Evidence for Great Holocene earthquakes along the outer coast of Washington State. *Science*, *236*(4804), 942–944. https://doi.org/10.1126/science.236.4804.942

Baba, T., Tanioka, Y., Cummins, P. R., & Uhira, K. (2002). The slip distribution of the 1946 Nankai earthquake estimated from tsunami inversion using a new plate model. *Physics of the Earth and Planetary Interiors*, *132*(1–3), 59–73. https://doi.org/10.1016/S0031-9201(02)00044-4

Barrientos, S. E., & Ward, S. N. (1990). The 1960 Chile earthquake: Inversion for slip distribution from surface deformation. *Geophysical Journal International*, *103*, 589–598.

Bassett, D., & Watts, A. (2015). Gravity anomalies, crustal structure, and seismicity at subduction zones: 1. Seafloor roughness and subducting relief. *Geochemistry, Geophysics, Geosystems*, *16*, 1508–1540. https://doi.org/10.1002/2014GC005685.Key

Beck, S., Barrientos, S., Kausel, E., & Reyes, M. (1998). Source characteristics of historic earthquakes along the central Chile subducntion zone. *Journal of South American Earth Sciences*, *11*(2), 115–129.

Beck, S. L., & Christensen, D. H. (1991). Rupture process of the February 4, 1965, Rat Islands Earthquake. *Journal of Geophysical Research*, *96*(B2), 2205. https://doi.org/10.1029/90JB02092

Beck, S. L., & Ruff, L. J. (1987). Rupture process of the Great 1963 Kurile Islands earthquake sequence: Asperity interaction and multiple event rupture. *Journal of Geophysical Research*, *92*(B13), 14,123–14,138.

Beck, S. L., & Ruff, L. J. (1989). Great earthquakes and subduction along the Peru trench. *Physics of the Earth and Planetary Interiors*, *57*(3–4), 199–224. https://doi.org/10.1016/0031-9201(89)90112-X

Becker, J. J., Sandwell, D. T., Smith, W. H. F., Braud, J., Binder, B., Depner, J., et al. (2009). Global bathymetry and elevation data at 30 arc seconds resolution: SRTM30_PLUS. *Marine Geodesy*, *32*(4), 355–371. https://doi.org/10.1080/01490410903297766

Beroza, G., Rial, J. A., & McNally, K. C. (1984). Source mechanisms of the June 7, 1982 Ometepec, Mexico earthquake. *Geophysical Research Letters*, *11*(8), 689–692.

Bilek, S. L. (2010). Invited review paper: Seismicity along the South American subduction zone: Review of large earthquakes, tsunamis, and subduction zone complexity. *Tectonophysics*, *495*(1–2), 2–14. https://doi.org/10.1016/j.tecto.2009.02.037

Bilek, S. L., Schwartz, S. Y., & DeShon, H. R. (2003). Control of seafloor roughness on earthquake rupture behavior. *Geology*, *31*(5), 455–458. https://doi.org/10.1130/0091-7613(2003)031<0455:COSROE>2.0.CO;2

Bilham, R., Engdahl, R., Feldl, N., & Satyabala, S. P. (2005). Partial and complete rupture of the Indo-Andaman plate boundary 1847–2004. *Seismological Research Letters*, *76*(3), 299–311. https://doi.org/10.1785/gssrl.76.3.299

Boyd, T. M., Engdahl, E. R., & Spence, W. (1995). Seismic cycles along the Aleutian arc: Analysis of seismicity from 1957 through 1991. *Journal of Geophysical Research*, *100*(B1), 621–644. https://doi.org/10.1029/94JB02641

Brizzi, S., Sandri, L., Funiciello, F., Corbi, F., Piromallo, C., & Heuret, A. (2018). Multivariate statistical analysis to investigate the subduction zone parameters favoring the occurrence of giant megathrust earthquakes. *Tectonophysics*, *728–729*(January), 92–103. https://doi.org/10.1016/j.tecto.2018.01.027

Byrne, D. E., Sykes, L. R., & Davis, D. A. N. M. (1992). Great thrust earthquakes and aseismic slip along the plate boundary of the Makran subduction zone. *Journal of Geophysical Research*, *97*(91), 449–478.

Christensen, D. H., & Lay, T. (1988). Large earthquakes in the Tonga region associated with subduction of the Louisville Ridge. *Journal of Geophysical Research*, *93*(B11), 13,367–13,389.

Clague, J. J. (2002). The Earthquake threat in southwestern British Columbia: A geological perspective. *Natural Hazards*, *26*, 7–34. https://doi.org/10.1023/A:1015208408485

Clévédé, E., Bukchin, B., Favreau, P., Mostinskiy, A., Aoudia, A., & Panza, G. F. (2012). Long-period spectral features of the Sumatra-Andaman 2004 earthquake rupture process. *Geophysical Journal International*, *191*(3), 1215–1225. https://doi.org/10.1111/j.1365-246X.2012.05482.x

Cloos, M. (1992). Thrust-type subduction-zone earthquakes and seamount asperities: A physical model for seismic rupture. *Geology*, *20*, 601–604.

Comte, D., Eisenberg, A., Lorca, E., Pardo, M., Ponce, L., Saragoni, R., et al. (1986). The 1985 central Chile earthquake: A repeat of previous great earthquakes in the region? *Science*, *233*(4762), 449–453. https://doi.org/10.1126/science.233.4762.449

Contreras-Reyes, E., & Carrizo, D. (2011). Control of high oceanic features and subduction channel on earthquake ruptures along the Chile-Peru subduction zone. *Physics of the Earth and Planetary Interiors*, *186*(1–2), 49–58. https://doi.org/10.1016/j.pepi.2011.03.002

Contreras-Reyes, E., Flueh, E. R., & Grevemeyer, I. (2010). Tectonic control on sediment accretion and subduction off south central Chile: Implications for coseismic rupture processes of the 1960 and 2010 megathrust earthquakes. *Tectonics*, *29*, TC6018. https://doi.org/10.1029/2010TC002734

Contreras-Reyes, E., Maksymowicz, A., Lange, D., Grevemeyer, I., Muñoz-Linford, P., & Moscoso, E. (2017). On the relationship between structure, morphology and large coseismic slip: A case study of the M_W 8.8 Maule, Chile 2010 earthquake. *Earth and Planetary Science Letters*, *478*, 27–39. https://doi.org/10.1016/j.epsl.2017.08.028

Corbi, F., Funiciello, F., Brizzi, S., Lallemand, S., & Rosenau, M. (2017). Control of asperities size and spacing on seismic behavior of subduction megathrusts. *Geophysical Research Letters*, *44*(16), 8227–8235. https://doi.org/10.1002/2017GL074182

Das, S., & Kostrov, B. V. (1990). Inversion for seismic slip rate history and distribution with stabilizing constraints: Application to the 1986 Andreanof Islands earthquake. *Journal of Geophysical Research*, *95*(B5), 6899. https://doi.org/10.1029/JB095iB05p06899

Das, S., & Watts, A. B. (2009). Effect of subducting seafloor topography on the rupture characteristics of great subduction zone earthquakes. *Subduction Zone Geodynamics*, 103–118. https://doi.org/10.1007/978-3-540-87974-9

Dominguez, S., Lallemand, S. E., Malavieille, J., & Von Huene, R. (1998). Upper plate deformation associated with seamount subduction. *Tectonophysics*, *293*(3–4), 207–224. https://doi.org/10.1016/S0040-1951(98)00086-9

Duong, N. A., Thuy, N. N., Kimata, F., Meilano, I., & Yen, L. T. H. (2009). Assessment of bathymetry effects on tsunami propagation in Vietnam. *Advances in Natural Sciences*, *10*(4), 457–468.

Fedotov, S. A., Solomatin, A. V., & Chernyshev, S. D. (2011). A long-term earthquake forecast for the Kuril-Kamchatka arc for the period from September 2010 to August 2015 and the reliability of previous forecasts, as well as their applications. *Journal of Volcanology and Seismology*, *5*(2), 75–99. https://doi.org/10.1134/S0742046311020023

Franco, A., Lasserre, C., Lyon-Caen, H., Kostoglodov, V., Molina, E., Guzman-Speziale, M., et al. (2012). Fault kinematics in northern Central America and coupling along the subduction interface of the Cocos Plate, from GPS data in Chiapas (Mexico), Guatemala and El Salvador. *Geophysical Journal International*, *189*(3), 1223–1236. https://doi.org/10.1111/j.1365-246X.2012.05390.x

Geersen, J., Ranero, C. R., Barckhausen, U., & Reichert, C. (2015). Subducting seamounts control interplate coupling and seismic rupture in the 2014 Iquique earthquake area. *Nature Communications*, *6*, 8267. https://doi.org/10.1038/ncomms9267

Goebel, T. H. W., Kwiatek, G., Becker, T. W., Brodsky, E. E., & Dresen, G. (2017). What allows seismic events to grow big?: Insights from *b*-value and fault roughness analysis in laboratory stick-slip experiments. *Geology*, *45*(9), 815–818. https://doi.org/10.1130/G39147.1

Goldfinger, C., Nelson, C. H., Morey, A. E., Joel, E., Patton, J., Karabanov, E., et al. (2012). Turbidite event history — Methods and implications for Holocene paleoseismicity of the Cascadia subduction zone. *U.S. Geological Survey Professional Paper*, *1661–F* (170 pp.). Retrieved from http://pubs.usgs.gov/pp/pp1661f/

Gutscher, M.-A., & Peacock, S. M. (2003). Thermal models of flat subduction and the rupture zone of great subduction earthquakes. *Journal of Geophysical Research*, *108*(B1), ESE 2–1–ESE 2–16. https://doi.org/10.1029/2001JB000787

Hartzell, S., & Langer, C. (1993). Importance of model parameterization in finite fault inversions—Application to the 1974 M_W 8.0 Peru earthquake. *Journal of Geophysical Research*, *98*(B12), 22,123–22,134. https://doi.org/10.1029/93jb02453

Hashimoto, C., Noda, A., Sagiya, T., & Matsu'ura, M. (2009). Interplate seismogenic zones along the Kuril–Japan trench inferred from GPS data inversion. *Nature Geoscience*, *2*(2), 141–144. https://doi.org/10.1038/ngeo421

Hayes, G. P. (2017). The finite, kinematic rupture properties of great-sized earthquakes since 1990. *Earth and Planetary Science Letters*, *468*(June 2016), 94–100. https://doi.org/10.1016/j.epsl.2017.04.003

Heise, W., Caldwell, T. G., Bannister, S., Bertrand, E. A., Ogawa, Y., Bennie, S. L., & Ichihara, H. (2017). Mapping subduction interface coupling using magnetotellurics: Hikurangi margin, New Zealand. *Geophysical Research Letters*, *44*, 9261–9266. https://doi.org/10.1002/2017GL074641

Henstock, T. J., McNeill, L. C., Bull, J. M., Cook, B. J., Gulick, S. P. S., Austin, J. A., et al. (2016). Downgoing plate topography stopped rupture in the A.D. 2005 Sumatra earthquake. *Geology*, *44*(1), 71–74. https://doi.org/10.1130/G37258.1

Heuret, A., Conrad, C. P., Funiciello, F., Lallemand, S., & Sandri, L. (2012). Relation between subduction megathrust earthquakes, trench sediment thickness and upper plate strain. *Geophysical Research Letters*, *39*, L05304. https://doi.org/10.1029/2011GL050712

Heuret, A., Lallemand, S., Funiciello, F., Piromallo, C., & Faccenna, C. (2011). Physical characteristics of subduction interface type seismogenic zones revisited. *Geochemistry, Geophysics, Geosystems*, *12*, Q01004. https://doi.org/10.1029/2010GC003230

Hirata, K., Geist, E., Satake, K., Tanioka, Y., & Yamaki, S. (2003). Slip distribution of the 1952 Tokachi-Oki earthquake (M 8.1) along the Kuril Trench deduced from tsunami waveform inversion. *Journal of Geophysical Research*, *108*(B4), 2196. https://doi.org/10.1029/2002JB001976

Holdahl, S. R., & Sauber, J. (1994). Coseismic slip in the 1964 Prince William Sound earthquake: A new geodetic inversion. *Pure and Applied Geophysics PAGEOPH*, *142*(1), 55–82. https://doi.org/10.1007/BF00875968

Ji, C., Wald, D. J., & Helmberger, D. V. (2002). Source description of the 1999 Hector Mine, California, earthquake, part I: Wavelet domain inversion theory and resolution analysis. *Bulletin of the Seismological Society of America*, *92*(4), 1192–1207. https://doi.org/10.1785/0120000916

Johnson, J. M., & Satake, K. (1994). Rupture extent of the 1938 Alaskan earthquake as inferred from tsunami waveforms. *Geophysical Research Letters*, *21*(8), 733–736.

Johnson, J. M., & Satake, K. (1999). Asperity distribution of the 1952 Great Kamchatka earthquake and its relation to future earthquake potential in Kamchatka. *Pure and Applied Geophysics*, *154*(3–4), 541–553. https://doi.org/10.1007/s000240050243

Johnson, J. M., Tanioka, Y., Ruff, L. J., Satake, K., Kanamori, H., & Sykes, L. R. (1994). The 1957 great Aleutian earthquake. *Pure and Applied Geophysics PAGEOPH*, *142*(1), 3–28. https://doi.org/10.1007/BF00875966

Kelleher, J., & McCann, W. (1976). Buoyant zones, great earthquakes, and unstable boundaries of subduction. *Journal of Geophysical Research*, *81*(26), 4885–4896.

Kelleher, J., Savino, J., Rowlett, H., & McCann, W. (1974). Why and where great thrust earthquakes occur along island arcs. *Journal of Geophysical Research*, *79*(32), 4889–4899. https://doi.org/10.1029/JB079i032p04889

Kelleher, J., Sykes, L., & Oliver, J. (1973). Possible criteria for predicting earthquake locations and their application to major plate boundaries of the Pacific and the Caribbean. *Journal of Geophysical Research*, *78*(14), 2547. https://doi.org/10.1029/JB078i014p02547

Kelleher, J. A. (1972). Rupture zones of large South American earthquakes and some predictions. *Journal of Geophysical Research*, *77*(11), 2087. https://doi.org/10.1029/JB077i011p02087

Kodaira, S., Takahashi, N., Nakanishi, A., Miura, S., & Kaneda, Y. (2000). Subducted seamount imaged in the rupture zone of the 1946 Nankaido earthquake. *Science*, *289*(5476), 104–106. https://doi.org/10.1126/science.289.5476.104

Kopp, H. (2013). Invited review paper: The control of subduction zone structural complexity and geometry on margin segmentation and seismicity. *Tectonophysics*, *589*, 1–16. https://doi.org/10.1016/j.tecto.2012.12.037

LaFemina, P., Dixon, T. H., Govers, R., Norabuena, E., Turner, H., Saballos, A., et al. (2009). Fore-arc motion and Cocos Ridge collision in Central America. *Geochemistry, Geophysics, Geosystems*, *10*, Q05S14. https://doi.org/10.1029/2008GC002181

Lallemand, S. (2016). Philippine Sea Plate inception, evolution, and consumption with special emphasis on the early stages of Izu-Bonin-Mariana subduction. *Progress in Earth and Planetary Science*, *3*(1), 15. https://doi.org/10.1186/s40645-016-0085-6

Lallemand, S., Culotta, R., & Von Huene, R. (1989). Subduction of the Daiichi Kashima seamount in the Japan Trench. *Tectonophysics*, *160*(1–4), 231–241. https://doi.org/10.1016/0040-1951(89)90393-4

Lallemand, S., & Heuret, A. (2017). Subduction zones parameters. In *Reference module in Earth systems and environmental sciences* (pp. 1–15). New York: Elsevier Inc. https://doi.org/10.1016/B978-0-12-409548-9.09495-1

Lallemand, S., Peyret, M., van Rijsingen, E., Arcay, D., & Heuret, A. (2018). Roughness characteristics of oceanic seafloor prior to subduction in relation to the seismogenic potential of subduction zones. *Geochemistry, Geophysics, Geosystems*, *19*, 1–26. https://doi.org/10.1029/2018GC007434

Landgrebe, T. C. W., & Müller, R. D. (2015). Uncovering the relationship between subducting bathymetric ridges and volcanic chains with significant earthquakes using geophysical data mining. *Australian Journal of Earth Sciences*, *62*(2), 171–180. https://doi.org/10.1080/08120099.2015.1003145

Lapusta, N., & Rice, J. R. (2003). Nucleation and early seismic propagation of small and large events in a crustal earthquake model. *Journal of Geophysical Research*, *108*(B4), 2309. https://doi.org/10.1029/2001JB000793

Lay, T. (2017). A review of the rupture characteristics of the 2011 Tohoku-oki M_W 9.1 earthquake. *Tectonophysics*, *733*(September 2017), 4–36. https://doi.org/10.1016/j.tecto.2017.09.022

Lay, T., & Kanamori, H. (1980). Earthquake doublets in the Solomon Islands. *Physics of the Earth and Planetary Interiors*, *21*(4), 283–304. https://doi.org/10.1016/0031-9201(80)90134-X

Lay, T., & Kanamori, H. (1981). An asperity model of large earthquake sequences. *Earthquake Prediction*, *4*, 579–592.

Lay, T., Kanamori, H., & Ruff, L. (1982). The asperity model and the nature of large subduction zone earthquakes. *Earthquake Prediction Research*, *1*, 3–71.

Loveless, J. P., Pritchard, M. E., & Kukowski, N. (2010). Testing mechanisms of seismic segmentation with slip distributions from recent earthquakes along the Andean margin. *Tectonophysics*, *495*, 15–33. https://doi.org/10.1016/j.tecto.2009.05.008

Mai, P. M., & Thingbaijam, K. K. S. (2014). SRCMOD: An online database of finite-fault rupture models. *Seismological Research Letters*, *85*(6), 1348–1357. https://doi.org/10.1785/0220140077

Manaker, D. M., Calais, E., Freed, A. M., Ali, S. T., Przybylski, P., Mattioli, G., et al. (2008). Interseismic plate coupling and strain partitioning in the Northeastern Caribbean. *Geophysical Journal International*, *174*(3), 889–903. https://doi.org/10.1111/j.1365-246X.2008.03819.x

Matsuda, T., Ota, Y., Ando, M., & Yonekura, N. (1978). Fault mechanism and recurrence time of major earthquakes in southern Kanto district, Japan, as deduced from coastal terrace data. *Bulletin of the Geological Society of America*, *89*(11), 1610–1618. https://doi.org/10.1130/0016-7606(1978)89<1610:FMARTO>2.0.CO;2

Mendoza, C., & Hartzell, S. (1989). Slip distribution of the 19 september 1985 Michoacan, Mexico, earthquake: Near-source and teleseismic constraints. *Bulletin of the Geological Society of America*, *79*(3), 655–669.

Mendoza, C., Hartzell, S., & Monfret, T. (1994). Wide-band analyisis of the 3 March 1985 Central Chile Earthquake: Overall source process and rupture history. *Bulletin of the Seismological Society of America*, *84*(2), 269–283.

Métois, M., Socquet, A., & Vigny, C. (2012). Interseismic coupling, segmentation and mechanical behavior of the central Chile subduction zone. *Journal of Geophysical Research*, *117*, B03406. https://doi.org/10.1029/2011JB008736

Mochizuki, K., Yamada, T., Shinohara, M., Yamanaka, Y., & Kanazawa, T. (2008). Weak interplate coupling by seamounts and repeating *M* approximately 7 earthquakes. *Science*, *321*(5893), 1194–1197. https://doi.org/10.1126/science.1160250

Moeremans, R. E., & Singh, S. C. (2014). Seismic evidence of continental margin influence on the NinetyEast Ridge in the Bay of Bengal. *Geophysical Research Letters*, *41*, 7143–7150. https://doi.org/10.1002/2014GL061598

Moeremans, R. E., & Singh, S. C. (2015). Fore-arc basin deformation in the Andaman-Nicobar segment of the Sumatra-Andaman subduction zone: Insight from high-resolution seismic reflection data. *Tectonics*, *34*(8), 1736–1750. https://doi.org/10.1002/2015TC003901

Morgan, P. M., Feng, L., Meltzner, A. J., Lindsey, E. O., Tsang, L. L. H., & Hill, E. M. (2017). Sibling earthquakes generated within a persistent rupture barrier on the Sunda megathrust under Simeulue Island. *Geophysical Research Letters*, *44*, 2159–2166. https://doi.org/10.1002/2016GL071901

Müller, R. D., & Landgrebe, T. C. W. (2012). The link between great earthquakes and the subduction of oceanic fracture zones. *Solid Earth*, *3*(2), 447–465. https://doi.org/10.5194/se-3-447-2012

Natawidjaja, D. H., Sieh, K., Ward, S. N., Cheng, H., Edwards, R. L., Galetzka, J., & Suwargadi, B. W. (2004). Paleogeodetic records of seismic and aseismic subduction from central Sumatran microatolls, Indonesia. *Journal of Geophysical Research*, *109*, L14316. https://doi.org/10.1029/2003JB002398

Newcomb, K. R., & McCann, W. R. (1987). Seismic history and seismotectonics of the Sunda Arc. *Journal of Geophysical Research*, *92*, 421–439. https://doi.org/10.1029/JB092iB01p00421

Nishenko, S. P. (1991). Circum-Pacific seismic potential: 1989–1999. *Pure and Applied Geophysics PAGEOPH*, *135*(2), 169–259. https://doi.org/10.1007/BF00880240

Nishizawa, A., Kaneda, K., Watanabe, N., & Oikawa, M. (2009). Seismic structure of the subducting seamounts on the trench axis: Erimo Seamount and Daiichi-Kashima Seamount, northern and southern ends of the Japan Trench. *Earth, Planets and Space*, *61*(3), e5–e8. https://doi.org/10.1186/BF03352912

Nocquet, J.-M., Jarrin, P., Vallée, M., Mothes, P. A., Grandin, R., Rolandone, F., et al. (2016). Supercycle at the Ecuadorian subduction zone revealed after the 2016 Pedernales earthquake. *Nature Geoscience*, *10*(December 2016), 145–149. https://doi.org/10.1038/ngeo2864

Nocquet, J.-M., Villegas-Lanza, J. C., Chlieh, M., Mothes, P. a., Rolandone, F., Jarrin, P., et al. (2014). Addendum: Motion of continental slivers and creeping subduction in the northern Andes. *Nature Geoscience*, *7*(8), 612–612. https://doi.org/10.1038/ngeo2217

Ohnaka, M. (2000). A physical scaling relation between the size of an earthquake and its nucleation zone size. *Pure and Applied Geophysics*, *157*(11), 2259–2282. https://doi.org/10.1007/PL00001084

Okal, E. A. (2012). The south of Java earthquake of 1921 September 11: A negative search for a large interplate thrust event at the Java Trench. *Geophysical Journal International*, *190*(3), 1657–1672. https://doi.org/10.1111/j.1365-246X.2012.05570.x

Okal, E. A., Borrero, J., & Synolakis, C. E. (2004). The earthquake and tsunami of 1865 November 17: Evidence for far-field tsunami hazard from Tonga. *Geophysical Journal International*, *157*(1), 164–174. https://doi.org/10.1111/j.1365-246X.2004.02177.x

Okal, E. A., & Hartnady, C. J. (2009). The South Sandwich Islands earthquake of 27 June 1929: Seismological study and inference on tsunami risk for the South Atlantic. *South African Journal of Geology*, *112*(3–4), 359–370. https://doi.org/10.2113/gssajg.112.3-4.359

Pacheco, J., Singh, S. K., Domínguez, J., Hurtado, A., Quintanar, L., Jiménez, Z., et al. (1997). The October 9, 1995 Colima-Jalisco, Mexico earthquake (Mw 8): An aftershock study and a comparison of this earthquake with those of 1932. *Geophysical Research Letters*, *24*(17), 2223–2226.

Park, S. C., & Mori, J. (2007). Are asperity patterns persistent? Implication from large earthquakes in Papua New Guinea. *Journal of Geophysical Research*, *112*, B03303. https://doi.org/10.1029/2006JB004481

Peacock, S. M., & Hyndman, R. D. (1999). Hydrous minerals in the mantle wedge and the maximum depth of subduction thrust earthquakes. *Geophysical Research Letters*, *26*(16), 2517–2520.

Pelayo, A. M., & Wiens, D. A. (1990). The November 20,1960 Peru tsunami earthquake: Source mechanism of a slow event. *Geophysical Research Letters*, *17*(6), 661–664. https://doi.org/10.1029/GL017i006p00661

Perez, O. J. (2000). Kuril Islands Arc: Two seismic cycles of great earthquakes during which the complete history of seismicity ($M_s > 6$) is observed. *Bulletin of the Seismological Society of America*, *90*(4), 1096–1100.

Ranero, C. R., Grevemeyer, I., Sahling, H., Barckhausen, U., Hensen, C., Wallmann, K., et al. (2008). Hydrogeological system of erosional convergent margins and its influence on tectonics and interplate seismogenesis. *Geochemistry, Geophysics, Geosystems*, *9*, Q03S04. https://doi.org/10.1029/2007GC001679

Ranero, C. R., & von Huene, R. (2000). Subduction erosion along the Middle America convergent margin. *Nature*, *404*(April), 748–752.

Rivera, L., Sieh, A., Natawidjaja, K., Helmberger, D. H., & Anonymous, D. V. (2002). A comparative study of the 1935 and 1984 Sumatran subduction earthquakes. *Eos, Transactions of the American Geophysical Union*, *81*(48), 913. https://doi.org/10.1785/0120010106

Robinson, D. P., Das, S., & Watts, A. B. (2006). Earthquake rupture stalled by a subducting fracture zone. *Science*, *312*(2006), 1203–1204. https://doi.org/10.1126/science.1125771

Ruff, L., & Kanamori, H. (1980). Seismicity and the subduction zone process. *Physics of the Earth and Planetary Interiors*, *23*, 240–252.

Ruff, L. J. (1989). Do trench sediments affect great earthquake occurrence in subduction zones? *Pure and Applied Geophysics PAGEOPH*, *129*(1–2), 263–282. https://doi.org/10.1007/BF00874629

Ruff, L. J., & Miller, A. D. (1994). Rupture process of large earthquakes in the northern Mexico subduction zone. *Pure and Applied Geophysics PAGEOPH*, *142*(1), 101–172. https://doi.org/10.1007/BF00875970

Ruh, J. B., Sallarès, V., Ranero, C. R., & Gerya, T. (2016). Crustal deformation dynamics and stress evolution during seamount subduction: High-resolution 3-D numerical modeling. *Journal of Geophysical Research: Solid Earth*, *121*, 6880–6902. https://doi.org/10.1002/2014JB011489

Saffer, D. M. (2017). Mapping fluids to subduction megathrust locking and slip behavior. *Geophysical Research Letters*, *44*, 9337–9340. https://doi.org/10.1002/2017GL075381

Saffer, D. M., & Tobin, H. J. (2011). Hydrogeology and mechanics of subduction zone forearcs: Fluid flow and pore pressure. *Annual Review of Earth and Planetary Sciences*, *39*(1), 157–186. https://doi.org/10.1146/annurev-earth-040610-133408

Satake, K. (2003). Fault slip and seismic moment of the 1700 Cascadia earthquake inferred from Japanese tsunami descriptions. *Journal of Geophysical Research*, *108*(B11), 2535. https://doi.org/10.1029/2003JB002521

Satake, K. (2015). Geological and historical evidence of irregular recurrent earthquakes in Japan. *Philosophical Transactions of the Royal Society A: Mathematical, Physical and Engineering Sciences*, *373*(2053), 20140375. https://doi.org/10.1098/rsta.2014.0375

Scholl, D. W., Kirby, S. H., von Huene, R., Ryan, H., Wells, R. E., & Geist, E. L. (2015). Great ($\geq M_W$8.0) megathrust earthquakes and the subduction of excess sediment and bathymetrically smooth seafl oor. *Geosphere*, *11*(2), 236–265. https://doi.org/10.1130/GES01079.1

Scholz, C. H., & Campos, J. (2012). The seismic coupling of subduction zones revisited. *Journal of Geophysical Research*, *117*, B05310. https://doi.org/10.1029/2011JB009003

Scholz, C. H., & Small, C. (1997). The effect of seamount subduction on seismic coupling. *Geology*, *25*(6), 487–490. https://doi.org/10.1130/0091-7613(1997)025<0487:TEOSSO>2.3.CO;2

Schwartz, S. Y., & Ruff, L. J. (1985). The 1968 Tokachi-Oki and the 1969 Kurile Islands earthquakes: Variability in the rupture process. *Journal of Geophysical Research*, *90*, 8613. https://doi.org/10.1029/JB090iB10p08613

Schwartz, S. Y., & Ruff, L. J. (1987). Asperity distribution and earthquake occurrence in the southern Kurile Islands arc. *Physics of the Earth and Planetary Interiors*, *49*(1–2), 54–77. https://doi.org/10.1016/0031-9201(87)90132-4

Singh, S. K., Suárez, G., & Domínguez, T. (1985). The Oaxaca, Mexico, earthquake of 1931: Lithospheric normal faulting in the subducted Cocos plate. *Nature*, *317*(5), 56–58.

Smith, W. H. F., & Sandwell, D. T. (1997). Global sea floor topography from satellite altimetry and ship depth soundings. *Science*, *277*, 1956–1962. https://doi.org/10.1126/science.277.5334.1956

Sparkes, R., Tilmann, F., Hovius, N., & Hillier, J. (2010). Subducted seafloor relief stops rupture in South American great earthquakes: Implications for rupture behaviour in the 2010 Maule, Chile earthquake. *Earth and Planetary Science Letters*, *298*(1–2), 89–94. https://doi.org/10.1016/j.epsl.2010.07.029

Stein, S., & Okal, E. A. (2007). Ultralong period seismic study of the December 2004 Indian Ocean earthquake and implications for regional tectonics and the subduction process. *Bulletin of the Seismological Society of America*, *97*(1A), S279–S295. https://doi.org/10.1785/0120050617

Stein, S., & Okal, E. A. (2011). The size of the 2011 Tohoku earthquake need not have been a surprise. *Eos, Transactions of the American Geophysical Union*, *92*(27), 227–228. https://doi.org/10.1146/annurev

Storchak, D. A., Di Giacomo, D., Bondár, I., Engdahl, E. R., Harris, J., Lee, W. H. K., et al. (2013). Public release of the ISC-GEM global instrumental earthquake catalog (1900–2009). *Seismological Research Letters*, *84*(5), 810–815. https://doi.org/10.1785/0220130034

Strasser, F. O., Arango, M. C., & Bommer, J. J. (2010). Comparison of seismicity rates in the New Madrid and Wabash Valley seismic zones. *Seismological Research Letters*, *81*(6), 951–954. https://doi.org/10.1785/gssrl

Swenson, J. L., & Beck, S. L. (1996). Historical 1942 Ecuador and 1942 Peru subduction earthquakes, and earthquake cycles along Colombia-Ecuador and Peru subduction segments. *Pure and Applied Geophysics*, *146*(1), 67–101. https://doi.org/10.1007/BF00876670

Sykes, L. R. (1971). Aftershock sequences of great earthquakes, seismicity gaps, and erathquake prediction for Alaska and Aleutians. *Journal of Geophysical Research*, *76*(32), 8021–8041.

Tajima, F., & Kanamori, H. (1985). Aftershock area expansion and mechanical heterogeneity of fault zone within subduction zones. *Geophysical Research Letters*, *12*(6), 345–348. https://doi.org/10.1029/GL012i006p00345

Tanioka, Y., & Satake, K. (2001). Detailed coseismic slip distribution of the 1944 Tonankai earthquake estimated from tsunami waveforms. *Geophysical Research Letters*, *28*(6), 1075–1078.

Theunissen, T., Font, Y., Lallemand, S., & Liang, W. T. (2010). The largest instrumentally recorded earthquake in Taiwan: Revised location and magnitude, and tectonic significance of the 1920 event. *Geophysical Journal International*, *183*(3), 1119–1133. https://doi.org/10.1111/j.1365-246X.2010.04813.x

Theunissen, T., Lallemand, S., Font, Y., Gautier, S., Lee, C. S., Liang, W. T., et al. (2012). Crustal deformation at the southernmost part of the Ryukyu subduction (East Taiwan) as revealed by new marine seismic experiments. *Tectonophysics*, *578*(June), 10–30. https://doi.org/10.1016/j.tecto.2012.04.011

Wang, K., & Bilek, S. L. (2011). Do subducting seamounts generate or stop large earthquakes? *Geology*, *39*(9), 819–822. https://doi.org/10.1130/G31856.1

Wang, K., & Bilek, S. L. (2014). Invited review paper: Fault creep caused by subduction of rough seafloor relief. *Tectonophysics*, *610*, 1–24. https://doi.org/10.1016/j.tecto.2013.11.024

Wang, K., & Tréhu, A. M. (2016). Invited review paper: Some outstanding issues in the study of great megathrust earthquakes—The Cascadia example. *Journal of Geodynamics*, *98*, 1–18. https://doi.org/10.1016/j.jog.2016.03.010

Weatherall, P., Marks, K. M., Jakobsson, M., Schmitt, T., Tani, S., Arndt, J. E., et al. (2015). A new digital bathymetric model of the world's oceans. *Earth and Space Science*, *2*, 331–345. https://doi.org/10.1002/2015EA000107

Wessel, P., Smith, W. H. F., Scharroo, R., Luis, J., & Wobbe, F. (2013). Generic mapping tools: Improved version released. *Eos, Transactions American Geophysical Union*, *94*(45), 409–410. https://doi.org/10.1002/2013EO450001

Wyss, M. (1976). Local sea level changes before and after the Hyuganada, Japan, Earthquakes. *Journal of Geophysical Research*, *81*(29), 5315–5321.

Yamanaka, Y., & Kikuchi, M. (2004). Asperity map along the subduction zone in northeastern Japan inferred from regional seismic data. *Journal of Geophysical Research*, *109*, B07307. https://doi.org/10.1029/2003JB002683

Ye, L., Kanamori, H., & Lay, T. (2018). Global variations of large megathrust earthquake rupture characteristics. *Science Advances*, *4*, 1–8. https://doi.org/10.1126/sciadv.aao4915

Ye, L., Lay, T., Kanamori, H., & Rivera, L. (2016). Rupture characteristics of major and great ($M_W \geq 7.0$) megathrust earthquakes from 1990 to 2015: 1. Source parameter scaling relationships. *Journal of Geophysical Research: Solid Earth*, *122*, 826–844. https://doi.org/10.1002/2016JB013608

Yokota, Y., Ishikawa, T., Watanabe, S., Tashiro, T., & Asada, A. (2016). Seafloor geodetic constraints on interplate coupling of the Nankai Trough megathrust zone. *Nature*, *534*(7607), 4–6. https://doi.org/10.1038/nature17632

Yue, H., & Lay, T. (2013). Source rupture models for the M_W 9.0 2011 Tohoku earthquake from joint inversions of high-rate geodetic and seismic data. *Bulletin of the Seismological Society of America*, *103*(2 B), 1242–1255. https://doi.org/10.1785/0120120119

Zielke, O., Galis, M., & Mai, P. M. (2017). Fault roughness and strength heterogeneity control earthquake size and stress drop. *Geophysical Research Letters*, *44*, 777–783. https://doi.org/10.1002/2016GL071700